Simulations of compressible flows associated with internal combustion engines

by

Olle Bodin

February 2013
Technical Reports from
Royal Institute of Technology
KTH Mechanics
SE-100 44 Stockholm, Sweden

Akademisk avhandling som med tillstånd av Kungliga Tekniska Högskolan i Stockholm framlägges till offentlig granskning för avläggande av teknologie doktorsexamen Fredagen den 8/2 2013 kl 10:00 i sal F3, Lindstedtsvägen 26, Kungliga Tekniska Högskolan, Vallhallavägen 79, Stockholm.

©Olle Bodin 2013
Universitetsservice US–AB, Stockholm 2013

Simulations of compressible flows associated with internal combustion engines

Olle Bodin 2013,
KTH Mechanics
SE-100 44 Stockholm, Sweden

Abstract

Vehicles with internal combustion (IC) engines fueled by hydrocarbon compounds have been used for more than 100 years for ground transportation. During these years and in particular the last decade, the environmental aspects of IC engines have become a major political and research topic. Following this interest, the emissions of pollutants such as NO_x, CO_2 and unburned hydrocarbons (UHC) from IC engines have been reduced considerably.

Yet, there is still a clear need and *possibility* to improve engine efficiency while further reducing emissions of pollutants. The maximum efficiency of IC engines used in passenger cars is no more than 40% and considerably less than that under part load conditions. One way to improve engine efficiency is to utilize the energy of the exhaust gases to turbocharge the engine. While turbocharging is by no means a new concept, its design and integration into the gas exchange system has been of low priority in the power train design process. One expects that the rapidly increasing interest in efficient passenger car engines would mean that the use of turbo technology will become more widespread.

The flow in the IC-engine intake manifold determines the flow in the cylinder prior and during the combustion. Similarly, the flow in the exhaust manifold determines the flow into the turbine, and thereby the efficiency of the turbocharging system.

In order to reduce NO_x emissions, exhaust gas recirculation (EGR) is used. As this process transport exhaust gases into the cylinder, its efficiency is dependent on the gas exchange system in general. The losses in the gas exchange system are also an issue related to engine efficiency. These aspects have been addressed up to now rather superficially. One has been interested in global aspects (e.g. pressure drop, turbine efficiency) under *steady state* conditions.

In this thesis, the flow in the exhaust port and close to the valve as well as in the exhaust manifold is studied. Since the flow in the port can be transonic, we study first the numerical modeling of such a flow in a more simple geometry, namely a bump placed in a wind tunnel. Large-Eddy Simulations of internal transonic flow have been carried out. The results show that transonic flow in general is very sensitive to small disturbances in the boundary conditions. Flow in the wind tunnel case is always highly unsteady in the transonic flow regime with self excited shock oscillations and associated with that

also unsteady boundary-layer separation. The interaction between separation zone and shock dynamics was carried out by one-, and two-point correlations as well as dynamic mode decomposition (DMD). A clear connection between separation bubble dynamics and shock oscillation was found. To investigate sensitivity to periodic disturbances the outlet pressure in the wind tunnel case was varied periodically at rather low amplitude. These low amplitude oscillations caused hysteretic behavior in the mean shock position and appearance of shocks of widely different patterns.

The study of a model exhaust port shows that at realistic pressure ratios, the flow is transonic in the exhaust port. Furthermore, two pairs of vortex structures are created downstream of the valve plate by the wake behind the valve stem and by inertial forces and the pressure gradient in the port. These structures dissipate rather quickly. The impact of these structures and the choking effect caused by the shock on realistic IC engine performance remains to be studied in the future.

The flow in a heavy-duty exhaust manifold was studied under steady and engine-like boundary conditions. At all conditions, significantly unsteady flow is generated in the manifold and at the inlets to the turbine and EGR cooler. The inflow to the turbine is dominated by a combination of the blow-down pulse coming from one cylinder, and the scavenging pulse from another at the firing frequency.

Descriptors: Transonic flow, Hysteresis, Shock/boundary-layer interaction, Exhaust valve, Large Eddy Simulation, Exhaust manifold.

Preface

This PhD thesis consist of two parts. The first part gives an overview of the automotive internal combustion engine, compressible flows, computational methods and a short summary of the results. The second part consists of six papers, which are adjusted to comply with the present thesis format for consistency. The content of the papers have been updated and include minor refinements as compared to the published versions. In Chapter 9 of the first part of the thesis the contribution of the respondent to the papers is stated.

February 2013, Stockholm
Olle Bodin

Contents

Abstract iii

Preface v

Chapter 1. Introduction 1

Chapter 2. Internal combustion engines 3
2.1. Operation principles 4
2.2. Pollutants 5
2.3. Performance and reduction of emissions 6

Chapter 3. Compressible flows 11
3.1. Basics 11
3.2. Governing equations for compressible flows 12
3.3. Compressible flow effects 13

Chapter 4. Turbulent flow modeling and computational aspects 23
4.1. Turbulence 23
4.2. Turbulence modeling 26

Chapter 5. Data analysis and post-processing techniques 33
5.1. Flow uniformity 33
5.2. Power spectral density 33
5.3. Correlation techniques 34
5.4. Vortex detection 35
5.5. Flow decomposition methods 36

Chapter 6. Flows under consideration 43
6.1. Transonic channel 43
6.2. Transonic flow in an model IC engine exhaust valve port 43

6.3. Heavy-duty exhaust manifold and port 45
6.4. Computational aspects 49

Chapter 7. Results and discussion 58
7.1. Transonic channel flow 58
7.2. Transonic flow in an model IC engine exhaust valve port 67
7.3. Flow in a heavy-duty exhaust manifold 69

Chapter 8. Summary and conclusions 76
8.1. Transonic channel flow 76
8.2. Transonic flow in a model IC engine exhaust valve port 77
8.3. Flow in a heavy-duty exhaust manifold 78

Chapter 9. Papers summary and authors contributions 79

Acknowledgments 82

Bibliography 83

92

94

96

98

100

Part I

Overview and summary

CHAPTER 1

Introduction

Vehicles with internal combustion engines fueled by liquid hydrocarbon of some sort has been a significant transport mode for about 100 years. During the later part of the evolution towards present day, the focus of development has steadily moved towards reducing the environmental impact of transport. This is done by reducing the harmful emissions from the engine, both in the form of chemical and acoustic pollution, and increasing engine efficiency.

An obvious way of decreasing the environmental impact of a vehicle is to reduce the amount of fuel it consumes, increase the efficiency of the vehicle. For reciprocal internal combustion engines, the efficiency with regard to output power versus fuel energy content is typically less than 40%. The main loss sources in the engine are cooling and flow-related.

One way to make an engine more efficient is to use the energy of the exhaust gases to turbocharge it, and thereby reduce the flow losses. While turbocharging is by no means a new concept and is widely used, the rapidly increasing interest in efficient passenger cars mean that the use of turbo technology will become more widespread. An example of this is so-called downsizing, where a turbocharger is employed to enable smaller-displacement engines to be used.

Even with turbocharging however, much of the exhaust energy is still lost. Between the cylinder and the turbocharger turbine the exhaust gases pass through first the exhaust port containing the exhaust valve, and then the exhaust manifold. Along this path, as much as 30% of the available energy at the exhaust valve is lost, of course depending on the specific engine and operating conditions. Clearly, the gas flow in this part of the engine can have a large impact on the total efficiency of the engine

The work presented here is aimed at deepening the knowledge of the flow in internal combustion engines through detailed simulations of the flow in the exhaust port. More specifically, the transonic flow in a duct with a bump, a simple exhaust port and the flow in a heavy-duty exhaust manifold are analyzed.

The approach taken in this work is to use the more geometrically simple example of internal and transonic flow over a bump to evaluate the analysis

of the complicated flow phenomena found in unsteady transonic flows. For this geometry, experimental data is available making it possible to evaluate the computational results by comparison to the experiments. As a second step, we have allowed unsteadiness in the flow conditions by varying the outlet static pressure. The results show clearly the intricate character of transonic flows; namely, the presence of time-varying complex shock systems and that the flow conditions under a given state of boundary conditions (BC) depends on flow history (i.e. the flow is hysteretic). Additionally, one encounters unsteady turbulent flow noting separated boundary layers with time dependent location and extent. The knowledge, analysis, and basic understanding together with similar methodology from the bump flow investigation is then used to investigate the transonic and unsteady flow in a model internal combustion engine exhaust port. The port geometry has a significantly more complex geometry resulting in new flow features that are not found in the case of the bump. Features are secondary flow due to centrifugal instability and wake effects behind the valve stem as well as their interaction. The final step was to investigate the flow in a heavy-duty exhaust manifold under engine-like boundary conditions with respect to the generation of turbine inflow conditions.

The unsteadiness of the shock in the transonic bump flow is a result of the interaction between the separating boundary layer and the shock. Acoustic disturbances in the flow are present but is not significantly affecting the dynamics of the shock motion. The shock position exhibit hysteresis when subjected to slowly varying outlet pressure because of varying shock Mach number in accelerating and decelerating flow.

For the exhaust port, two distinctive pairs of vortices are generated downstream of the valve by centrifugal instabilities in the port and by the wake behind the valve. These secondary flow structures are quite strong initially and, depending on the conditions downstream of the valve, are convected downstream in a more or less coherent fashion.

The dynamic inflow to the turbine from the exhaust manifold is dominated by two characteristic flow structures, detected by Proper Orthogonal Decomposition and Dynamic Mode Decomposition. The most energetic one is the main mass flow pulse consisting of both the blow-down pulse and the scavenging pulse coming from different cylinders. The second structure is the side-to-side pulse behavior caused by the manifold geometry.

CHAPTER 2

Internal combustion engines

This chapter presents a brief history of the automotive internal combustion engine and briefly describes some concepts and components that are important for the results of this thesis.

The history of the internal combustion (IC) engine dates back to the 17th century when the Dutch scientist Christiaan Huygens designed the first documented piston and cylinder engine (Galloway 2010). Huygens engine used gunpowder to evacuate the air under the piston and the engine work was done by the atmospheric pressure.

Experimentation and development of a multitude of engine designs and concepts followed during the 18th and 19th centuries. During the early history of the internal combustion engine, the main driver for development was the need for a smaller, lighter, and cheaper power source as an alternative to the steam engine.

In the mid-19th century, Alphonse Beau de Rochas realized that compressing the fuel/air mixture (charge) prior to ignition was essential to achieve higher efficiency in an internal combustion engine, Heywood (1988). Beau de Rochas did this in 1862 by outlining the conditions for maximum efficiency in an internal combustion engine (Heywood 1988):

- The largest possible cylinder volume with the smallest possible boundary surface
- The greatest possible working speed
- The greatest possible expansion ratio
- The greatest possible pressure at the beginning of expansion

A major breakthrough in the development of the internal combustion engine was achieved in 1876 when Nicolaus Otto realized the first four-stroke internal combustions engine[1]. This engine type was considerably smaller than the preceding engines, more than halving the weight for similar power output (Heywood 1988).

[1] Otto was the first to construct and build a functioning four-stroke engine in 1876 but the concept was described, and patented in 1862 by Alphonse Beau de Rochas (Heywood 1988).

Although already small and light compared to the steam engines, it was not until the end of the 19th century that internal combustion engines small and powerful enough to be used in a vehicle were built. Developed by Karl Benz, Gottlieb Daimler and Wilhelm Maybach (cca. 1886) these were part of the first generation of modern automotive internal combustion engines (Heywood 1988).

The basic layout of the reciprocating internal combustion engine, where the thermodynamic processes are being controlled by a crank and piston, has endured since the early designs. Other ideas have been tried with various levels of success (e.g. the gas turbine engine, Wankel engine) but the reciprocating internal combustion engine has been the dominant power source for road vehicles since the end of the 19th century. It is a simple, robust power source that can be manufactured with relative ease using non-exotic materials. It also has characteristics that suit the automotive application, such as good transient response.

The main drivers for development of commercial internal combustion engines today are increased efficiency and the reduction of regulated emissions.

2.1. Operation principles

The two main operating principles for an internal combustion engine with piston are the Otto, named after Nikolaus Otto, and the Diesel, named after Rudolf Diesel. In an Otto engine, the air/fuel charge is more or less mixed and then ignited by a high-energy electric discharge. This type of combustion id called *premixed* combustion and is mostly dependent on the flowfield of the air-fuel mixture. A Diesel engine on the other hand compresses the air charge and then injects fuel which is subsequently ignited by the high temperature and pressure within the combustion chamber. This combustion type is called *diffusion* combustion and is dependent on both in-cylinder flow field and injection characteristics.

Pressure-volume diagrams of idealized Otto, and Diesel cycles are plotted in Figure 2.1. The different combustion types in the two cycle types are here represented as constant-volume combustion in the Otto cycle, and constant pressure combustion in the Diesel cycle (for the idealized case). Also, an Otto engine may be used in throttled operation, which rise to the separate area under the main p-V curve. This area represent the pumping losses associated with the throttle. All engines must supply fresh air and fuel to the combustion and, subsequently, remove the combustion products. This process is collectively called gas exchange and is divided into four parts:

- Intake
- Compression
- Combustion
- Exhaust

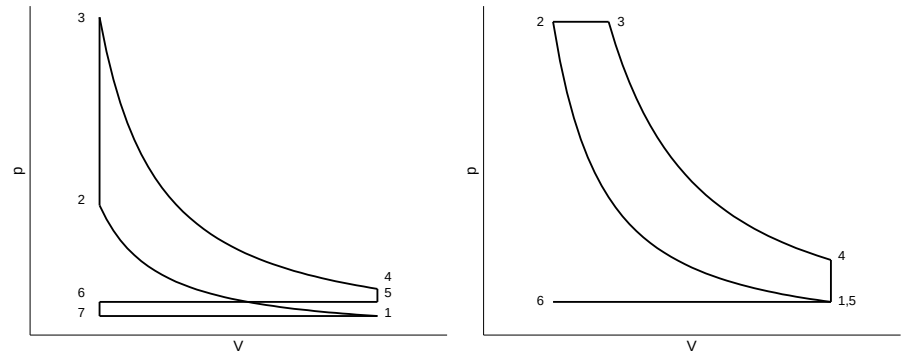

FIGURE 2.1. Left: p-V diagram for idealized throttled Otto cycle. 1-2 Isentropic compression, 2-3 Combustion, 3-4 Isentropic expansion, 4-5-6-7 Exhaust, 7-1 Intake. Right: p-V diagram for idealized Diesel cycle. 1-2 Isentropic compression, 2-3 Combustion, 3-4 Isentropic expansion, 4-5-6 Exhaust, 6-1 Intake.

A four-stroke engine cylinder does this process in two revolutions of the crank shaft and thus delivers power every second down stroke of the piston. This type of engine is the standard in a wide variety of applications (e.g. cars, trucks, buses), where versatility and low emission requirements are important. A two-stroke engine on the other hand manages the gas exchange process at every revolution of the crank shaft and delivers power every down stroke of the piston. One area where this type of engines is used is where high power density and mechanical simplicity are desired (e.g. chainsaws, small-capacity motorcycles, mopeds). The two-stroke engine typically mixes gasoline, lubrication oil and air causing significant problems with emissions. Another application for two-stroke engines are very large low-speed engines for use in, for example, ships. These are direct injection turbocharged Diesel engines with valves, which do not mix lubrication oil with air or fuel. Thus the emission related problems of the smaller two-stroke engines are avoided. In fact, these engine types are among the most efficient reciprocating engines built with a thermal efficiency in excess of 50% (MAN Diesel & Turbo 2012).

2.2. Pollutants

Regardless of fuel type, engine configuration, and operating principle the combustion process will generate combustion products. When referring to an internal combustion engine the products are called emissions. For simplification purposes, the very complex combustion process of an internal combustion engine fueled by petroleum can be described as an oxidation process (under high

pressure and temperature conditions) of a hydrocarbon such as Diesel or gasoline (C_xH_y or simply HC). From such a reaction will result the following pollutants: Nitrous oxides (NO_x), carbon dioxide (CO_2), carbon monoxide (CO), and hydrocarbons (HC). Also included are soot or particulate matter emissions which consist of larger particles (compared to gas molecules) of unburned hydrocarbons. These emissions adversely affect the environment and health of both humans and animals, both on short and long terms. For these reasons governments use legislations to force engine and vehicle manufacturers to continuously develop means to reduce the harmful emissions of their products.

2.3. Performance and reduction of emissions

Meeting the exhaust emissions regulations is absolutely necessary for an automotive manufacturer in order to sell their products. It is also clear that surpassing legislation has become a marketing point not only for very specialized, low-consumption, cars. Even in motor sports, hybrid technology and fuel restrictions are being introduced using environmental and efficiency arguments. The 2012 LeMans 24 hours endurance race was won by the hybrid Audi R18 e-tron. Audi used a turbocharged direct-injection Diesel engine with a particle filter together with a electromechanical flywheel system to store kinetic energy[2]. Formula 1 have decided that, from 2014, engines will have a reduced displacement from 2.4 L (V8) to 1.6 L (V6) and employ a turbocharger[3]. Fuel flow restrictions compared to the previous rules will be employed. Kinetic energy recovery systems will be allowed as well as exhaust energy recovery systems, connected to the turbocharger. Neither the Audi endurance racer, nor the future Formula 1 cars will be particularly friendly to the environment. However, the successful implementation of hybrid systems in race cars and the changes in the rules of one of the most prestigious motor sports (motivated by fuel consumption and efficiency) shows the commercial value of such arguments.

2.3.1. *Efficient gas exchange*

On the intake side of the gas exchange process, detailed knowledge of the flow field behavior is essential to ensure efficient combustion as the combustion process is highly dependent on the conditions in the cylinder prior to the actual combustion.

Some components of the inflow characteristics do survive to varying degrees during the compression phase of the engine. For example, the swirl (see Figure 2.2) generated at the intake port survives and may be enhanced by the compression (Heywood 1988) whereas the tumbling motion (see Figure 2.2)

[2]Usually called kinetic energy recovery system, KERS, these kind of systems can be used to recover energy from braking by transferring the forward momentum of the car to the flywheel.
[3]An example of downsizing, see 2.3.3

does not (Fogleman *et al.* 2004; Boree *et al.* 2002). This is the result of the

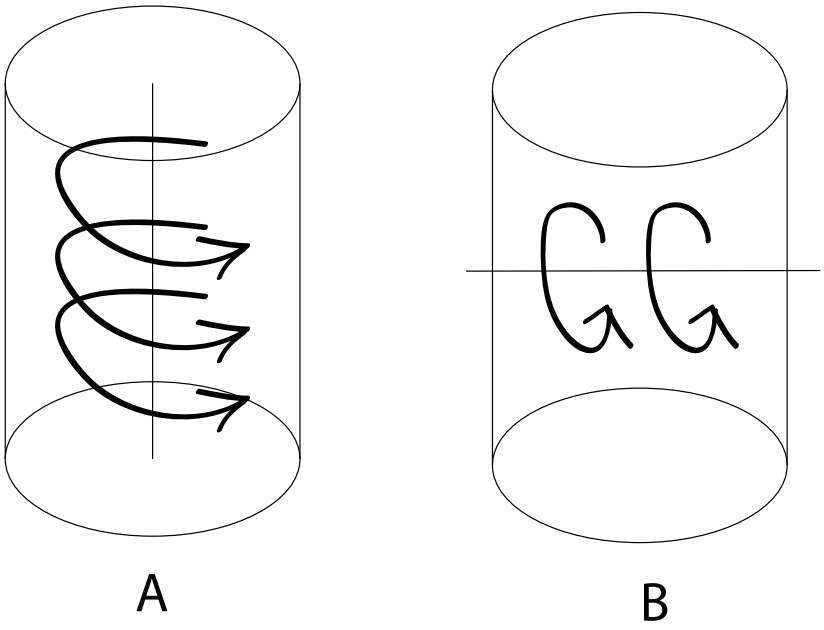

FIGURE 2.2. Inflow characteristics, large scale flow motion.
A: Swirl. B: Tumble

instability of some modes and the stability of others as well as the change of geometry caused by the compression.

Because of such effects and their impact on combustion stability, fuel consumption and pollutant formation, much work has been done to understand the flow in the intake ports and in-cylinder during the intake and combustion strokes see e.g. Valentino *et al.* (1993); Bicen *et al.* (1986); Yasar *et al.* (2006); Lee *et al.* (2005); Gault *et al.* (2004); Buschbeck *et al.* (2012). Compared to this, the exhaust ports have received much less attention.

During the exhaust phase, the engine must expel the products of combustion. Flow losses in the exhaust valve ports have a major impact on the efficiency of the gas exchange. The character of the flow at the exhaust port is quite different compared to that at the intake port due to the differences in pressure gradients. When the exhaust valve opens, the pressure difference between cylinder and exhaust port is on the order of 500 kPa, with a temperature difference of more than 300 K.

In addition to the flow losses, the heat transfer to the exhaust valves is an important aspect in the design of the exhaust valves and port. Incorrect assessment of the heat transfer can lead to structural failure and may also greatly complicate the assessment of downstream components such as the turbine or EGR cooler, which are dependent on the exhaust gas temperature.

The heat transfer problem in simple geometries, such as a boundary layer on a flat plate, has been studied in some detail and several engineering correlations exist. When these correlations are directly applied to more complicated flows, like valve ports and manifolds, they tend to fail predicting the heat flux correctly, see e.g. Caton & Heywood (1981). The reason behind the poor results is that the turbulent flow in these geometries is far from being fully developed or statistically stationary; conditions for which the models were calibrated. It was found that for an exhaust port the contributions to heat transfer from large scale fluid motion indeed dominate over the near-wall boundary layer (Caton & Heywood 1981). This means that, if one aims at predicting correctly the instantaneous heat transfer in such a situation by computational methods, the three-dimensional and time-dependent flow field must be considered and computed by an appropriate approach.

The manifold geometry will affect the flow losses and heat transfer generated while the gas passes through it. However, partly due to space constraints, the shape of an engine manifold cannot be totally decided by gas exchange efficiency. Manifolds should also be as small as possible as the manifold surface area directly affect heat losses from the exhaust gases to the manifold. Large heat losses are particularly harmful for transient response in turbocharged engines, see e.g. Galindo *et al.* (2004).

Another important aspect regarding manifold and port design is that, depending on the geometry, different secondary flow motions may be generated. Even a simple pipe bend will generate significant secondary flow motion (Sudo *et al.* 1998; Rutten *et al.* 2005; Kalpakli *et al.* 2011) and, as both the manifold and the exhaust port contain complex pipe shapes with bends and curvature, strong and unsteady secondary flows will be generated.

2.3.2. *Exhaust gas recirculation*

Emission regulations demand very small emissions of NO_x because of the severe problems associated with this pollutant.

The formation of NO_x during combustion occurs when nitrogen in the fuel reacts with the oxygen of the air at high temperatures in a complicated process[4]. Lowering the combustion temperature is therefore a sensible way of

[4]The principal reactions of NO formation from atmospheric nitrogen are described by the extended Zeldovich mechanism, see e.g. Heywood (1988)

decreasing NO_x formation and this can be achieved by recirculating exhaust gases to the inlet ports.

The exhaust gas recirculation (EGR) concept consists of recycling a fraction of exhaust gases through the intake manifold to replace some of the excess oxygen in the intake air. EGR lowers the peak combustion chamber temperature, as the exhaust gases contain less oxygen compared to fresh air. This will reduce the formation of NO_x during combustion. However, as exhaust gases are much hotter compared to the intake air, they must be cooled to preserve as much as possible of the volumetric efficiency of the engine.

An EGR cooler consists of many small diameter channels through which the fluid is transported. In these channels the heat transfer takes place. Naturally, the heat transfer process is dependent on both mass flow rate and the temperature of the fluid when it passes through these channels which is in turn dependent on the velocity and temperature distributions at the cooler inlet. As the flow conditions at the EGR cooler inlet are dependent on the flow in the manifold, increased understanding of the flow dynamics in exhaust manifolds is essential for efficient EGR coolers.

2.3.3. *Turbochargers*

The inventor of the turbocharger was the Swiss engineer Alfred Büchi who in 1905 patented a device which forced air into a Diesel engine by an exhaust-driven compressor. However, the turbocharger was first widely used during the First World War for increasing high-altitude performance of combat aircraft. Turbochargers increase the density of the air inducted into the combustion chamber by using the energy of the engine exhaust gases. This increase enable a larger mass of air in the cylinder, which in turn means that more fuel can be combusted.

A turbocharger will increase the power of an engine with a given displacement by making use of the energy of the exhaust, which is otherwise wasted. This will increase the power output relative to the engine displacement which can be used to achieve two different things: To simply make more power available or, to decrease the displacement while maintaining power output.

The latter approach is called downsizing and reduces the frictional losses, which are proportional to the engine displacement, compared to the larger non-turbocharged engine. A recent example of quite a substantial downsizing is the Ford EcoBoost, a 3 cylinder, 1 L displacement direct injection turbocharged gasoline engine producing 92 kW (125 hp).

It has been shown by several researchers that the efficiency of the turbocharger is dependent on the flow structures at the turbine inlet, see for example Ehrlich *et al.* (1997) and Hellström & Fuchs (2008). This dependence,

coupled with the need for increased efficiency which can be achieved by downsizing highlights the need to increase the understanding of the flow dynamics in exhaust manifolds.

2.3.4. *Close-coupled catalyst*

Catalytic converters are used in order to reduce the harmful emissions like carbon monoxide (CO), unburned hydrocarbons (HC), and nitrous oxides (NO_x) resulting from the combustion process within the IC engines. Catalytic converters require that their substrate has reached a certain temperature in order for the catalytic reactions to start. The time from engine cold start to a fully operating catalytic converter is called the light-off time and this is strongly dependent on the location of the catalytic converter in the exhaust system. If the catalytic converter is situated close to the engine (close-coupled catalyst or CCC), light-off time is reduced which in turn reduces the cold-start emissions. The location of a CCC on an exhaust manifold is very similar to the placement of a turbine and, just as the turbine the CCC efficiency is sensitive to the inflow structure, see e.g. Zygourakis (1989); Karvounis & Assanis (1993); Torino *et al.* (2003); Persoons *et al.* (2004); Salasc *et al.* (2005); Agrawal *et al.* (2012). Again, it is clear that understanding the flow dynamics in exhaust manifolds is essential in order to design efficient, low-emission engine systems.

CHAPTER 3

Compressible flows

This chapter begins by describing some basic physical properties and thermodynamics of fluids and then move on to a brief walkthrough of the conservation laws and governing equations in fluid mechanics.

3.1. Basics

Viscosity is the resistance of a fluid to deformation by shear or tensile stress. This fluid property comes from the interaction of it's constituting molecules which transfer momentum when they collide with each other. The collisions will thus diffuse momentum of the molecules through the fluid. For a Newtonian fluid, the stress has a linear dependence on the strain rate. The proportionality constant in this relation is fluid viscosity. To quantify viscosity in a continuum, consider the shear stress tensor of a Newtonian fluid:

$$\tau_{ij} = \mu \left(\frac{\partial u_i}{\partial x_j} + \frac{\partial u_j}{\partial x_i} - \frac{2}{3}\delta_{ij} \frac{\partial u_k}{\partial x_k} \right), \tag{3.1}$$

where μ is the dynamic viscosity of the fluid, u_i i=1,2,3 is the velocity, x_i i=1,2,3 are the Cartesian coordinates,

$$\frac{\partial}{\partial x_i}, \tag{3.2}$$

is the derivative in the coordinate direction i and

$$\delta_{ij} = \begin{cases} 0, & i \neq j \\ 1, & i = j \end{cases} \tag{3.3}$$

, is the Kronecker delta. The dynamic viscosity is quite strongly dependent on fluid temperature and is, for an ideal gas, usually modeled by Sutherland's formula,

$$\mu = \mu_0 \frac{T_0 + C}{T + C} \left(\frac{T}{T_0} \right)^{3/2}, \tag{3.4}$$

where C is the Sutherland's constant, T_0 is the reference temperature, T the fluid temperature and μ_0 is the reference viscosity. The bulk modulus, or elasticity, of a substance, K, is defined as:

$$K \equiv \rho \frac{dp}{d\rho} \quad \rightarrow \quad d\rho = \frac{\rho}{K} dp, \tag{3.5}$$

where ρ and p are the density and pressure of the substance, respectively. This relation provides a measure of the response, by density change, to a change in pressure. The bulk modulus of a (real) fluid is dependent on pressure and temperature and also on how the temperature varies during the compression process. For an ideal gas the equation of state is defined like:

$$p = \rho RT, \tag{3.6}$$

where p is the pressure, ρ is the density, T is the temperature and R is the specific gas constant. For an ideal gas, and an adiabatic (constant entropy, S) process, the bulk modulus can be written as

$$K_S = \gamma p, \qquad \gamma = \frac{c_p}{c_v} \tag{3.7}$$

where γ is the ratio of specific heats. Clearly, a fluid with a small K will be more strongly affected by pressure changes resulting in a larger change in density. Just as a comparison, the bulk modulus of two common fluids, water and air, are of the order $O(10^5)$ Pa and $O(10^9)$ Pa, respectively. Specific enthalpy is a property which represents the total energy of a system and it is defined as:

$$h = i + p/\rho, \tag{3.8}$$

where i is the internal energy which in an ideal gas $i = c_v(T)T$. The heat capacity, c_v, obey the relation $c_p - c_v = R$ for an ideal gas.

3.2. Governing equations for compressible flows

This section presents the governing equations for a viscous, compressible Newtonian fluid. No detailed derivations are shown here, the reader is referred to any book covering compressible flows, for example Versteeg & Malalasekera (2007). The law of conservation of mass for a compressible fluid flow is expressed as the continuity equation:

$$\frac{\partial \rho}{\partial t} + \frac{\partial}{\partial x_j}(\rho u_j) = 0, \tag{3.9}$$

where t is the time, and states that the change of mass per unit volume in a point is zero. Newton's second law states that the rate of change of momentum on a particle is equal to the sum of the forces acting on it. Formulating this law for a fluid gives the equation for conservation of momentum per unit volume (ρu_i) at a point,

$$\frac{\partial}{\partial t}(\rho u_i) + \frac{\partial}{\partial x_j}(\rho u_i u_j) = -\frac{\partial p}{\partial x_i} + \frac{\partial \tau_{ij}}{\partial x_j} + \rho f_i. \tag{3.10}$$

The terms from the left hand side of the equation represent the time rate of change of momentum (the first one) and the rate of change of momentum by convection (the second). On the right hand side are the pressure forces (first term), the effect of viscous stresses (second term), and the body forces (when

considered). The momentum equations are usually called the Navier-Stokes equations.

The first law of thermodynamics states that the rate of change of energy of a particle is equal to the rate of heat addition plus the work done on the particle. In fluid mechanics this is called the energy equation and for compressible flows can be formulated in terms of the total enthalpy of a particle:

$$\begin{aligned} \frac{\partial}{\partial t}\left(\rho h_0\right) + \frac{\partial}{\partial x_i}\left(\rho u_i h_0\right) &= \frac{\partial p}{\partial t} + \frac{\partial q_i}{\partial x_i} + \frac{\partial}{\partial x_i}\left(u_j \tau_{ij}\right) + \cdots \\ &\cdots + Q + W_{ext}, \end{aligned} \tag{3.11}$$

where

$$h_0 = h + \frac{1}{2}\left(u_1^2 + u_2^2 + u_3^2\right). \tag{3.12}$$

Above, q_i is the heat flux. W_{ext} is the work of external volume forces and Q is an external heat source. The heat flux q_i can be related with the local temperature gradient through Fourier's law of heat conduction,

$$q_i = -k\frac{\partial T}{\partial x_i}, \tag{3.13}$$

where k is the thermal conductivity. The left hand side of equation 3.11 contains the change in ρh_0 of the fluid particle due to time and convective transport. On the right hand side, the first term accounts for the work done on the particle generated by the time rate of change of the pressure, the second term represent the rate of heat addition to the particle while the third term accounts for work done by (viscous) surface forces.

3.3. Compressible flow effects

The compressibility of a fluid flow has a potentially large impact on the flow behavior. In many situations, flows of gases are compressible, i.e. has compressible effects. The main effect of compressibility in engineering flows is the work done by volume change against pressure forces. To illustrate the pressure work, consider the first law of thermodynamics for a reversible process in a closed system without flow,

$$dE = dQ - pdV. \tag{3.14}$$

In words, the equation states: The change in total energy of the system (dE) is equal to the heat added to the system (dQ) minus the work done by the system against the pressure forces (pdV). The consequence of this is that if the volume is decreased and no heat transfer out of the system is allowed ($dQ = 0$), the temperature will increase as it is proportional to the change in total energy. For a fluid flow this means that kinetic energy can be transferred to heat through this mechanism.

The most common way to verify if compressible effects are significant in a fluid flow, is to calculate the Mach number,

$$M = U/a \tag{3.15}$$

where U is the fluid velocity and a is the speed of sound in the medium of propagation. The speed of sound, a, is related to the bulk modulus like:

$$a = \sqrt{\frac{K}{\rho}} = \sqrt{\gamma RT}, \tag{3.16}$$

where the equation of state, equation 3.6, was used to form the last expression. Two Mach numbers have special significance. First, the limiting case of $M = 0$ is termed as the *incompressible limit*. For this case it has to be stressed that the incompressible limit differs in essence from low speed compressible flow, i.e. when the Mach number is small but not zero. Although the exact dividing value is not easily defined, most agree that a Mach number above 0.3 implies that the flow in question has significant compressible effects. One way of motivating this limit can be made by considering the isentropic relation,

$$\frac{\rho}{\rho_0} = \left(1 + \frac{\gamma - 1}{2} M^2\right)^{\frac{-1}{\gamma - 1}}, \tag{3.17}$$

where ρ_0 is the total, or stagnation density which is attained when the fluid is brought under the isentropic assumption to rest. If $M = 0.3$ is used in the above equation, the result is $\rho/\rho_0 \approx 0.956$ which means that the difference, or error, is less than 5% if the flow is considered to be incompressible i.e. have $\rho = \rho_0$. Classification like this is not enough though, as there are situations where compressible effects are important but not related to high Mach number flow, for example the compression stroke in an internal combustion engine, or acoustic radiation in low Mach number flow. The other limiting case is when the Mach number is unity, i.e. when the flow is *sonic*. For this case, the acoustic waves propagate at the same speed as the flow. For $M > 1$ the flow is termed *supersonic* because the flow speed exceeds the speed of sound in the medium of propagation and hence, no sound wave can propagate upstream. Flows that contain significant sub-, and supersonic regions, are called *transonic*. Transonic flow is present in many engineering applications. These include IC engine related flows, where the flow may be transonic past the intake and exhaust valves and in the turbocharger (both in the compressor and turbine components). For this reason, a deeper insight into shock theory is given in the following section.

3.3.1. *Shock theory*

Shocks are classified as either normal or oblique referring to their angle with respect to the incoming flow. As all shocks related to this work are oblique,

most of the discussion and background will concern oblique shocks of which normal shocks are a particular case. While normal shocks can be described in one dimension, oblique shocks are by their nature two or three-dimensional. Oblique shocks occur when a supersonic flow is redirected by for example a change in geometry such as a compression corner or a bump. The response of the flow is to change the direction of the stream lines as they pass through the oblique shock in order to accommodate the geometry change. Most textbooks that cover compressible flow, for example Anderson (2003), will contain derivations of the oblique shock relations. The resulting relations are presented here.

In all equations in this section, subscript 1 and 2 denote conditions pre- and post-shock, respectively. The relation between the shock angle θ, and streamline deflection angle δ as a function of incoming Mach number (M_1) and the ratio of specific heats ($\gamma = c_p/c_v$) is:

$$\tan(\delta) = 2\cot(\theta) = \left[\frac{M_1^2 \sin^2(\theta) - 1}{M_1^2(\gamma + \cos(2\theta)) + 2}\right]. \tag{3.18}$$

A property of oblique shocks is that the tangential velocity component is preserved as the streamline passes through the shock. Knowing this and the incoming flow velocity, one may calculate the normal component of the post-shock velocity with the help of equation (3.18).

The geometrical nature of the oblique shock relations allow creative graphical representations, one of which is the so called shock polar. This way of presenting the relations is best considered in a polar coordinate system where:

$$r(\phi) = \left[\frac{2v_1}{(\gamma + 1)}\right]\left[\frac{1}{M_1^2 \cos(\phi)} - \cos(\phi)\right]. \tag{3.19}$$

The formulation in equation (3.19) was found in Lee (1969) and is represented graphically in Figure 3.1, where $r(\phi)$ is the distance between O and Q, as a strophoid-like curve together with the oblique shock. Oblique shocks may be either *weak* or *strong*. Depending on the conditions of the medium the flow velocity downstream of the shock is supersonic (weak shock) or subsonic (strong shock). The intersections Q and Q' represent the weak and strong shock solutions, respectively, while Q'' represent the so called unphysical shock solution, see Lee (1969). The point S represent the normal shock solution while O is a Mach line or an infinitely weak oblique shock. Velocities before and after the shock are represented by the lengths of v_1 and v_2, where the latter can have different lengths depending on the shock type. Shock angle and streamline deflection angle are defined by the same notations as in equation (3.18).

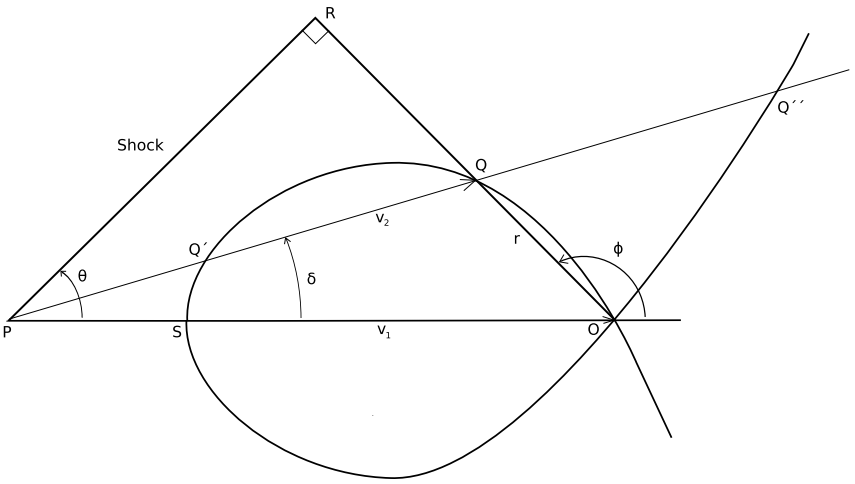

FIGURE 3.1. Oblique shock with shock polar.

3.3.1a. *Shock reflections.* In the vicinity of walls shocks are reflected. The reflection of an oblique shock can take place in two forms, either as a regular reflection (RR) or as a Mach reflection (MR). An illustration of the two different reflection types can be seen in Figure 3.2 where the fluid flow is from left to right and i, r, and s mark the incipient shock, the reflected shock, and the Mach stem, respectively. When the flow encounters the wedge, a shock is formed with an incipient angle that is dependent on both the incoming Mach number and the wedge angle.

If the flow Mach number increases from a state where the reflection is a RR, the angle will become smaller and the reflection will eventually transition from RR to MR. If the process is reversed and the incoming Mach number is reduced from a state where the reflection is a MR, the RR does not occur at the same incoming Mach number as the RR-MR transition (Hornung & Taylor 1982; Hornung & Robinson 1982; Ben-Dor *et al.* 2002; Ben-Dor 1999). This transition hysteresis is qualitatively illustrated in Figure 3.2, where the angle increases from left to right. The marked area in Figure 3.2 is called the *dual domain* due to the possibility of having either RR or MR in this range of shock angles. The dual domain is bounded by two angles, ω_{RR} and ω_{MR}, beyond which only one type of reflection is possible.

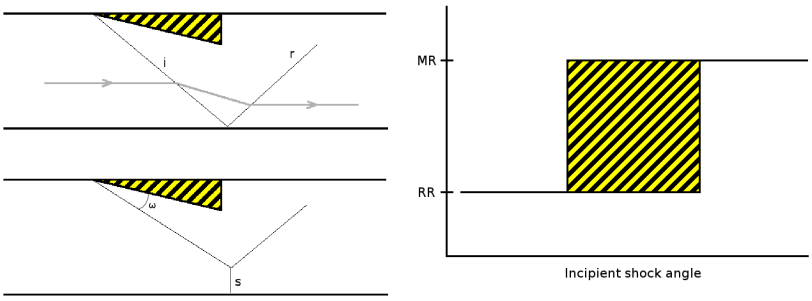

FIGURE 3.2. Left: Defining regular reflection (top), and Mach reflection (bottom). Right: Illustrating the hysteresis in the transition between Mach- and regular-reflection.

It turns out that the RR-MR transition is sensitive to disturbances so that in practice, the transition usually happens beyond ω_{RR} but before ω_{MR} while MR-RR transition usually occurs at ω_{RR}. However, it must be stressed that both reflections are stable and possible anywhere in the dual range although the MR is more insensitive to small disturbances in the hysteretic range.

3.3.2. *Shock/boundary-layer interactions*

The shocks that occur in transonic flows imply a (near) discontinuity in some of the flow variables such as density, pressure and shock normal velocity. In general, the boundary layer of a flow may separate if the pressure gradient is not favorable enough. This may happen at strong variations in the shape of the wall or due to a shock, which implies a steep pressure increase. Because of this, transonic internal flows often exhibit an interaction between shocks and boundary layer separation which is usually unsteady. The strong coupling between non-linear phenomena, shock shape and unsteady boundary layers is the reason for the complexity of this type of flow.

Transonic flows are in general sensitive to initial and boundary conditions (geometrical or flow conditions). This sensitivity is even more pronounced for internal flows where shocks may interact with wall boundary layers due to shock reflections and unsteady boundary layer separation. An experimental investigation by Liu & Squire (1988) considered the effect of a bump curvature and pressure ratio on the flow structure in transonic tunnel flow. The investigators used circular-arc bumps of varying radii under different driving pressure, such that the shock Mach number was in the range between 1 and 1.82. In this range one may find both weak and strong shocks, as well as flows with and without flow separation.

Three distinct types of boundary layer behavior were observed by Liu & Squire (1988): *(i)* fully attached flow, *(ii)* trailing edge separation, where the flow separated due to the adverse pressure gradient caused by the geometrical shape of the wall and, *(iii)* shock-induced separation, where the separation occurred behind the shock foot.

The pressure increase over a shock may be substantial when the shock-normal Mach number upstream of the shock is not very close to unity. Thus, shocks often induce adverse pressure gradients that lead to a thickening of the boundary layer. Such a thickening leads to a sharper change in the flow direction, which leads to an even stronger shock and hence, even stronger flow separation. Thus, it is easy to come to the conclusion that such flows are inherently unstable even for small perturbations.

The study of Liu & Squire (1988) showed that there exist a critical Mach number, M_c, where the separation change type from trailing-edge, to shock-induced and that this Mach number had the most extensive separation in the Mach number range under consideration for all bump curvatures.

Liu & Squire (1988) found that the general flow structure depended on the pressure ratio so that at a low ratio the shock first formed as a normal shock at the bump surface and as the pressure ratio increased gradually moved downstream and became stronger. Further increasing the pressure ratio resulted in that the shock extended over the whole tunnel, reaching the top wall of the tunnel where it was reflected as either a regular- or a Mach-reflection depending on the incipient shock angle. At even higher pressure ratio, the shock bifurcated, forming a λ-shock. The curvature of the bump effected the flow by increasing the shock strength with increasing curvature while for the smallest curvatures, the flow did not form a λ-shock at all. The critical Mach number was found to be nearly independent of the curvature of the circular arc bump ($M_c = 1.3$). If this Mach number was exceeded, the separation of the boundary layer was always shock-induced. The goal of the study of Liu & Squire (1988) was not to investigate the dynamics of the shock. However, indications of shock oscillations were found during this investigation.

3.3.2a. *Unsteady interaction.* In transonic flows, the shock position is often unsteady. The most commonly proposed mechanisms behind this are either acoustic interaction, shock/boundary-layer interaction or a combination of both.

The acoustic interaction scenario involves acoustic waves interacting with the shock in a transonic wind tunnel and was investigated by Bogar *et al.* (1983) among others. Bogar *et al.* (1983) reports that this phenomenon occurs when the shock Mach number was low enough such that the flow remains attached. The mechanism of the shock motion for this flow could then be described using (linear and one-dimensional) acoustic theory. As a side note to this result,

in supersonic shock/boundary-layer interaction without separation (Poggie & Smits 2001), the shock unsteadiness is completely dependent on the structures of the incoming boundary layer. In supersonic flow, the acoustic interaction is not possible. However, this result indicates that depending on the strength of the acoustic interaction, the incoming boundary layer may affect the shock dynamics.

For stronger shocks, when the flow may have a separated boundary layer, this type of acoustic mechanism for shock unsteadiness could be present but is overwhelmed by other perturbations in transonic shock/boundary-layer interaction (SBLI) (Salmon *et al.* 1983). This type of flow is associated with large-scale and low-frequency movement of the entire shock system both for transonic, and supersonic (Kistler 1964) flows.

The structures in the incoming boundary layer have been investigated in supersonic SBLI with strong shock-induced boundary layer separation. Burst-sweep events (Thomas *et al.* 1994), elongated regions of high and low speed fluid (Ganapathisubramani *et al.* 2007, 2009), fullness of velocity profile (Beresh *et al.* 2002; Wu & Martín 2007; Humble *et al.* 2009) and imposed perturbations with a velocity scale of the order U_τ, the friction velocity (Dussauge & Piponniau 2008) have all been considered. The conclusion however, is that, although shock position will be affected by the incoming boundary layer, the effect is very small and does not lead to the large-scale movement of the shock which was observed.

As the flow passes the shock there is a strong deceleration, primarily in the streamwise component of the velocity. This causes a strong increase in the streamwise velocity fluctuations and a large increase in the turbulence production at the shock which is further enhanced when the flow separates. Due to this strong perturbation, the properties of the incoming boundary layer upstream of the shock will have negligible influence on the free shear layer of the separation (Délery 1983).

Because of this, the dynamics of the separation bubble are likely to affect shock system movement. The effects of separation bubble dynamics on shock motion have been investigated by e.g. Kistler (1964); Thomas *et al.* (1994); Wu & Martín (2007). A strong correlation between large scale behavior in the separation zone, like the growth-burst sequence and movement of the reattachment point, and low frequency shock movement was found for all these cases.

Dussauge *et al.* (2006) compiled results from several different flow cases and researchers and suggested that they are to some extent similar. The authors defined the dimensionless shock motion frequency analogous to subsonic separated flows, as: $St_L = f_s L/U_e$, where f_s is the shock frequency, U_e is the external velocity, and L is the separation length. The shock frequency is defined by finding the maximum of $fG(f)$, where $G(f)$ is the PSD of pressure

fluctuations near the shock foot. For the cases examined in Dussauge *et al.* (2006), the characteristic shock frequency does not collapse in a strict manner but St_L typically falls between 0.02 and 0.05. Dussauge & Piponniau (2008) argue that the absence of a strict collapse for the characteristic shock frequency is to be expected if the source of the shock motion is flow-, and case-dependent.

In conclusion, the literature suggests that the unforced unsteadiness in transonic SBLI can be separated into two scenarios:

- No boundary layer separation. Cause of unsteadiness is a combination of the structure of incoming boundary layer and acoustic interaction between shock and some boundary.
- Boundary layer separation. Cause of unsteadiness is primarily the interaction between shock and the separation zone. Acoustics and the incoming boundary layer have only small effects.

A more detailed literature survey can be found in Chapter 9, paper 5.

3.3.2b. *Forced shock movement.* Due to the unsteady behavior of the shock, it is natural to investigate the behavior of the system when it is subjected to periodic perturbations. The possibility of controlling the shock motion and strength by careful choice of the perturbations can be an important tool in certain applications. One may apply the knowledge of such behavior to for example transonic wings, where the fluctuating forces may cause structural problems, decrease the efficiency of the wing or cause excessive noise.

Many investigations of periodic forcing in bump flow exist, for example Galli *et al.* (2005) where the outlet pressure in the transonic wind tunnel was perturbed by a rotating elliptical shaft to create a sinusoidal-like variation in the pressure downstream of the bump. Because the shock position was highly dependent on the outlet pressure a disturbance of the natural oscillation of the shock is created. Galli *et al.* (2005) found that damping the shock oscillations was possible by an appropriate choice of perturbation frequency, but did not report any attempts at amplifying it. Furthermore, Galli *et al.* (2005) found that the shock oscillation amplitude was inversely dependent on the perturbation frequency so that an increase in frequency lead to a decrease in amplitude.

In an investigation by Salmon *et al.* (1983), forcing was induced by a rotating device set into the tunnel wall at a frequency 38% above the frequency corresponding to the peak amplitude in the shock displacement spectra. The results and conclusions of the work by Salmon *et al.* (1983) were that no direct coupling between the natural oscillation of the shock and the forced perturbation could be observed. It was suggested that this could be explained by the broadband nature of the shock oscillation compared to the tonal nature of

the perturbation. The authors also highlighted that the reason for the natural oscillations in the case of strong shocks and shock-induced separation was the boundary layer perturbations. Furthermore, that transverse propagation (normal to the boundary layer) of these perturbations was an important part of the mechanism behind the natural oscillations of the strong shock.

An extensive investigation of forced flow by periodic perturbations in the same geometry and facility as Salmon *et al.* (1983) was conducted by Sajben *et al.* (1984). The same forcing method as in Salmon *et al.* (1983) was used but, with a much wider frequency range, including the natural frequency of the shock oscillation. Just like Salmon *et al.* (1983) and Bogar *et al.* (1983), two distinct flow configurations corresponding to weak and strong shocks were found.

For weak shocks, the natural shock oscillation spectra had two peaks. One of them corresponded to the acoustic interaction between the shock and the outflow boundary that could be described by streamwise propagation of plane waves. The other peak was explained through the perturbations that were created in the unseparated boundary layer when subjected to an adverse pressure gradient. The natural shock oscillation in the case of strong shocks was believed to be caused by turbulence, which excited perturbations that propagated both in the core flow and in the boundary layers. Only one peak was present in the shock spectra for the strong shock case and the acoustic interaction peak was not evident. Although the flow likely contained plane acoustic waves propagating back and fourth in the main flow direction, these acoustic modes were weak and their trace could hardly be observed in the otherwise turbulent flow.

Sajben *et al.* (1984) used one-dimensional acoustic theory to predict the motion of the shock. This simple model gave quite accurate results for the weak-shock case but failed completely to predict the strong shock case. The failure of the one-dimensional approach was the result of neglecting the boundary layer and other viscous effects.

The investigation by Sajben *et al.* (1984) failed to excite any resonant behavior in the shock oscillation in the weak and strong shock cases. The proposed explanation for this was that the modes responsible for the natural oscillation were not exited by the forced perturbations, which were close to plane waves propagating along the length of the diffuser. This explanation is most logical for the strong shock case, where there was no peak in the shock motion spectra associated with acoustic modes. For the weak shock case, the peak in the shock motion spectra associated with acoustics was not the main mode. The diffuser geometry was described as two-dimensional, having a two-parameter set of natural modes in a strict acoustic sense. However, the presence of the boundary layer, especially in the strong shock case, is likely to increase the real number of modes. The exact mode that is responsible for the natural shock

oscillation was not identified but the conclusion was that the plane acoustic waves were not a likely candidate as the driving mechanism for either case.

The reflective properties of the shock with respect to velocity and pressure perturbations are important as it determines the upstream boundary condition when the flow is choked. The downstream boundary in both experiments and simulations is often more or less reflective and in the case of perturbed flow, is also the source of the perturbations. Sajben *et al.* (1984) found that the reflective properties of the shock were dependent on the property considered, flow characteristics and if a forced perturbation was present in the flow. Depending on these, the reflection could vary between an almost total reflection in a "closed end" fashion, a reflection coefficient[1] of 1, and zero. As many other properties of shocks, the reflective behavior cannot be easily explained, or modeled, for other than weak shocks and pressure perturbations. Strong shocks and their strong coupling to boundary layer dynamics make the reflective properties difficult to quantify in general.

3.3.3. *Hysteresis*

Hysteresis may occur in any non-linear system and implies that a system can attain a distinct number of states depending on the path taken to get to the state. The non-linearity of the Navier-Stokes imply the possibility of hysteresis.

An example, not directly related to the present work, is the stall characteristic of certain airfoils where the stall angle does not coincide with the angle of boundary layer reattachment. In the transition between regular reflection and Mach reflection, hysteresis can be observed because of the existence of the dual domain where both reflections are possible. The transition angle is dependent on the path to it, see e.g. Ben-Dor *et al.* (2002)).

Another example of hysteresis in transonic flows is the mean position of the shock in bump flow with steady state boundary conditions, but possibly with different initial conditions. Such behavior has been reported by e.g. Moroianu *et al.* (2005). In this investigation, hysteresis in the shock position is observed when very low-frequency perturbations are applied while keeping the flow in the quasi-steady regime. Having covered some basics of compressible fluid dynamics, the next chapter will deal with simulation and modeling of fluid flows and turbulence.

[1] Defined as the ratio of the amplitudes of the reflected wave and the incident wave.

CHAPTER 4

Turbulent flow modeling and computational aspects

The equations describing fluid flow are the conservation of mass (Equation 3.9), momentum (Equation 3.10) and energy (Equation 3.11) together with a relation of state for the fluid (Equation 3.6). In general and for an arbitrary flow, this set of nonlinear partial differential equations can not be significantly simplified.

4.1. Turbulence

The flow at very low speeds is linear in character. As the speed increases, the importance of non-linear effects increases as well. The importance of non-linearity can be assessed by estimating the ratio between the convective and the viscous term in the momentum equation (the second and fourth terms in Equation 3.10, respectively). This ratio is called the Reynolds number[1],

$$Re = \frac{\rho U L}{\mu}, \tag{4.1}$$

where U is a characteristic velocity, L is a characteristic length and $\mu = \nu/\rho$ is the kinematic viscosity. Thus, at very small Re, like Stokes flow , the flow is dominated by viscous effects whereas for large Re it is dominated by convection.

Reynolds (1883, 1885) made studies of the flow of water in cylindrical pipes using dye visualization and found that depending on the value of the Reynolds number based on the pipe diameter, the flow behaved very differently. For low Reynolds numbers, the flow is parallel to the pipe walls, this is now called *laminar* flow. For high values of the Reynolds number, the flow is chaotic and full of eddies with varying sizes, what is now called *turbulent* flow[2]. Between these two regimes, there is a transitional phase where the flow does not correspond completely to either laminar or turbulent behavior.

The behavior of laminar flow is such that, depending on the Reynolds number, it is more or less sensitive to disturbances that causes transition to turbulent flow. One may define a *critical* Reynolds number, Re_c, where no

[1] First called so by Arnold Sommerfeld in 1908 (Rott 1990)

[2] Reynolds used the words *direct* and *sinusoidal* to describe the laminar flow and transition to turbulent flow (Reynolds 1883)

matter what the disturbance is, the flow will return to a laminar state. Above Re_c, transition to turbulence is possible by applying the right disturbance. Reynolds (1883, 1885) found that, for the circular pipes under consideration, Re_c was between 1900 and 2000.

In a similar fashion, one may define a Reynolds number where, no matter what the disturbance is, the laminar flow will always transition to turbulence, an upper limit for laminar flow. As one might imagine, finding this number requires that the naturally occurring disturbances of the experiment must be as small as possible (e.g. surface irregularities, vibrations). Reynolds (1883, 1885) found a limiting value of $Re = 13000$, for the circular pipes under consideration but noted that turbulent flow was observed at this Reynolds number previously and that great care must be taken for the flow to remain laminar[3]. Much higher Reynolds numbers were later reached by further reducing the disturbance levels in Reynolds equipment, see e.g. Rott (1990).

Turbulence can be described as a three-dimensional and time dependent interacting set of vortices with a range of scales from large ones, related to the global flow, to small ones, at the so called Kolmogorov scales. Closely linked with this is the so called *energy cascade*, where kinetic energy on average is transferred from the largest scales to the smallest, where it is dissipated and turned into heat. To illustrate the energy cascade, consider the model spectra for isotropic turbulence, see Figure 4.1, where the kinetic energy of the turbulent fluctuations are plotted versus their frequency. The kinetic energy of the turbulent flow structures is generated at the large scales in the energy containing rage (see Figure 4.1) where the *local* Reynolds number, is large, the characteristic scales for this range are:

$$U, L, t, \qquad Re = \frac{UL}{\nu} \tag{4.2}$$

Kinetic energy is on average transported through the inertial range (see Figure 4.1), where for isotropic turbulence at high Reynolds number, the energy of the turbulent fluctuations depend on the wave number like $E(f) \sim f^{-5/3}$. A characteristic lengthscale of the intertial range is the Taylor microscale,

$$\lambda \approx \left(\frac{10\nu k}{\varepsilon} \right)^{\frac{1}{2}}, \tag{4.3}$$

where k is the kinetic energy of the turbulent fluctuations. In the inertial range, characteristic scales are:

$$\lambda, \qquad Re_\lambda = \frac{U\lambda}{\nu} \tag{4.4}$$

[3]Later experiments (during the 1980's) using Reynolds original 1883 equipment could not reach a laminar flow at $Re = 13000$ and blamed the disturbances caused by modern traffic that were not present in 1883 (Rott 1990)

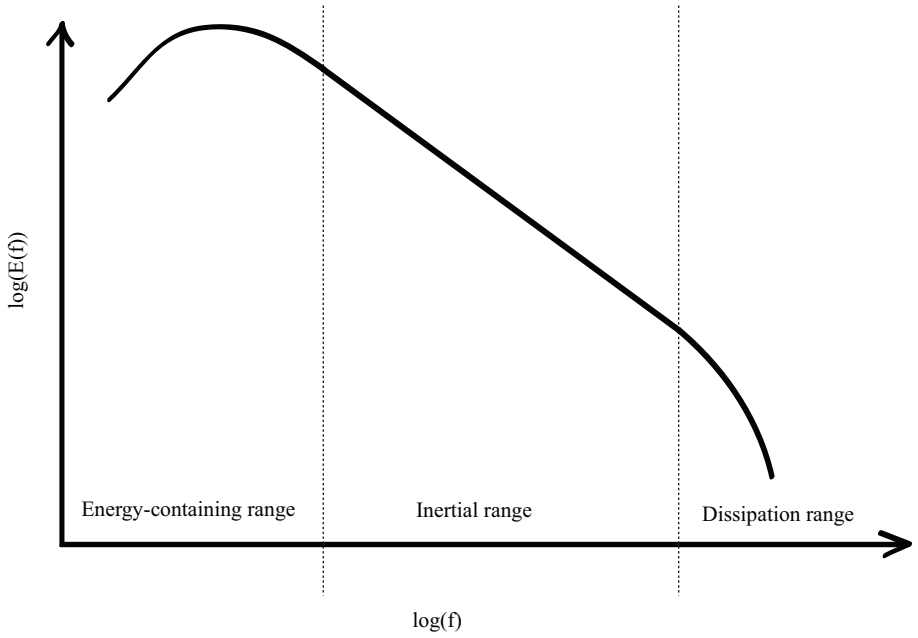

FIGURE 4.1. Model energy spectrum for high Reynolds number isotropic turbulence.

At the dissipation range (see Figure 4.1), the kinetic energy of the turbulent fluctuations are converted to heat, the characteristic scales are:

$$\eta_k, u_k, \tau_k, \qquad Re_{\eta_k} = \frac{\eta_k u_k}{\nu} = 1, \tag{4.5}$$

where the Kolmogorov scales, η_k, u_k, and τ_k are defined as:

$$\eta_k = \left(\frac{\nu^3}{\varepsilon}\right)^{\frac{1}{4}}, \quad \tau_k = \left(\frac{\nu}{\varepsilon}\right)^{\frac{1}{2}}, \quad u_k = (\nu\varepsilon)^{\frac{1}{4}}.$$

The kinetic energy of the turbulent fluctuations are on average transported in this fashion from the energy-containing range to the dissipation range. However, there is intermittent transfer in the other direction as well, a process which is commonly called *backscatter*.

The large scales in a flow are governed, and limited, by the geometry of the problem and are hence not universal. The smallest scales however, for large enough Reynolds numbers, have universal and geometry-independent behavior and hence lend themselves for modeling. The Reynolds number, Equation (4.1), is also a measure of the separation of these scales and in some sense the degree of complexity and character of the turbulence. An increase in Reynolds number by increasing flow speed for a given geometry means that more scales are included

in the small side of the cascade. Consider the Kolmogorov lengthscale, η_k. If the flow speed increases, the amount of energy in the flow increases, which will increase the rate of energy dissipation which in turn will reduce η_k if the viscosity is assumed constant. This decrease of the smallest scales with increasing Reynolds number has a significant impact on both fluid simulation and experimental measurements.

An important property of turbulent flows is their enhanced transport and mixing as compared to laminar flows. Increased transport of heat and species may be beneficial in certain applications while it may be undesired in others. For example, aircraft wings can be designed for laminar flow because of the reduced drag at cruise conditions. A turbulent flow over a wing can be beneficial tough, when an attached laminar flow is not possible, for example at high angle of attack when high-lift is required such as at landing and takeoff. Here, the rapid mixing of momentum in the boundary layer of the wing may eliminate the separation of the boundary layer and thereby wing stall. In premixed (Otto engine) combustion, the flame propagation speed and fuel/air mixture homogeneity is highly dependent on the turbulent flow in the cylinder, and intake port. For Diesel combustion, the interaction between the fuel spray and turbulent flow field in the cylinder is central to both efficiency and emissions formation.

Turbulence is a non-linear and chaotic phenomena where flow structures interact across a wide rage of scales. Turbulent flow is, as opposed to laminar, stable in the sense that disturbances will not cause the flow to change behavior drastically like the laminar-turbulent transition. It should also be pointed out that the flows may also have deterministic non-linear phenomena which is not turbulence and that all flow structures are not turbulence.

4.2. Turbulence modeling

The governing equations can, in principle, be solved using a numerical algorithm for all speeds and geometries. In order to achieve this, all the temporal and spatial scales of the flow should be resolved, i.e. from the largest integral scales (L, T) to the smallest Kolmogorov microscales (η_k, τ_k).Thus, it is essential to estimate these scales, either a priori or a posteriori. A rough estimate can be made through the Reynolds number, Equation (4.1).

The ratio between the smallest (Kolmogorov) scales and the largest (integral) scales goes, for very large Re, as $Re^{-3/4}$, whereas the corresponding ratio for the time scales goes as $Re^{-1/2}$. For numerical computations however, it is more relevant to consider the timescale obtained from the CFL number,

$$\frac{U\Delta t}{\Delta x} \leq 1 \quad \rightarrow \quad t_{CFL} = \frac{U}{\eta_k}. \tag{4.6}$$

The ratio between t_{CFL} and integral time scale goes like $Re^{-3/4}$. Thus, for a high Re, three-dimensional, turbulent flow one has to carry out computations that grow almost as Re^3. This makes such a direct approach (called Direct Numerical Simulation, DNS) limited to relatively small Re. For most engineering applications DNS cannot be carried out and one has to rely on a model to fill out the gap resulting from the lack of resolution.

Turbulence can be characterized by statistical properties such as mean, root mean square, higher statistical moments, probability density functions and spectra. Thus, it is natural to work with variables that express directly these statistical quantities. Equations for the mean of the original variables can be derived easily by averaging the basic equations and writing the instantaneous variables in terms of the mean and a fluctuating component. In contrast, DNS provides the instantaneous field which has to be processed in order to determine the statistical properties of the turbulent field.

The averaging process leads to a system of partial differential equations (PDE), the so called Reynolds Averaged Navier Stokes (RANS) equations, which resembles the governing equation system but has the addition of terms containing correlations of the fluctuating components (due to the non-linearity of the governing equations). The above mentioned terms cannot be expressed as function of mean quantities and have to be modeled. This difficulty is called the *closure problem* and the different expressions used to resolve the closure problem lead to different turbulence models. In the following subsections a brief introduction into some of the modeling approaches is given.

Common approaches to engineering turbulent flow calculations belong to one of the following categories:

- Large Eddy Simulation (LES)
- Reynolds Averaged Navier-Stokes (RANS)

Besides such formulations, there are also hybrid approaches such as Detached Eddy Simulation (DES) where LES and RANS are combined in various ways.

4.2.1. *Reynolds Averaged Navier-Stokes*

Reynolds Averaged Navier-Stokes is the most common way of dealing with turbulent flow computations, at least for engineering problems. This approach uses averaging of the instantaneous fields in the NSE to obtain an equation for the mean fields. Averaging is done by decomposing the instantaneous fields in the following way: $u_i \equiv U_i + u_i'$ and $p \equiv P + p'$ creating an average and a fluctuating part. If this decomposition is applied to the incompressible NSE,

the RANS equations are obtained as:

$$\frac{\partial U_i}{\partial x_i} = 0, \tag{4.7}$$

$$\frac{\partial U_i}{\partial t} + U_j \frac{\partial U_i}{\partial x_j} = \frac{1}{\rho}\frac{\partial P}{\partial x_i} + \frac{\partial}{\partial x_j}\left(2\nu S_{ij} - \overline{u_i' u_j'}\right). \tag{4.8}$$

In Equation 4.8, $S_{ij} \equiv (U_{i,j} + U_{j,i})/2$, the mean strain rate tensor. The last term in the momentum Equation 4.8, $\overline{u_i' u_j'}$, is called the Reynolds stress tensor and contains the additional stress on the mean field due to the turbulent fluctuations. The Reynolds stresses must be modeled in order to close the RANS system of equations and there are many ways to do this. The eddy viscosity assumption states that the turbulent stresses depend only on local phenomena. This assumption can be a reasonable approximation in simple shear flows (e.g. flat plate boundary layers, channel flows, or mixing layers). In highly three-dimensional flows or flows containing large-scale fluctuations (e.g. separation bubbles) the assumption is not equally reasonable. Examples of models based on the eddy viscosity (or Boussinesq) assumption include the Baldwin-Lomax zero-equation model or the Spalart-Almaras one-equation model, to name just a couple (see e.g. Wilcox (2006)). The most frequently used eddy viscosity based turbulence models within the RANS framework are the so called two-equation models. Among them are the $k - \varepsilon$ and the $k - \omega$ models, see e.g. Wilcox (2006).

Less commonly used in industrial applications are the Reynolds Stress Models (RSM), where the eddy viscosity assumption is replaced by a transport equation for the Reynolds stresses. This removes the assumption that the turbulent stresses are isotropic and dependent only on local quantities. The Reynolds Stress Models are in principle more general when compared to the eddy viscosity approach.

4.2.2. *Large Eddy Simulation*

If the scale content of a flow is not too wide (i.e. for low Re), DNS is applicable. For larger Reynolds numbers small scale structures are generated which makes the use of DNS prohibitively expensive. If the energy content and the dynamic importance of these scales are small however, one may still use the same approach as in DNS but refrain from resolving the smallest scales. This technique may be complemented by some model that accounts for the effects of the unresolved small scales on the resolved ones. This is the essence of Large Eddy Simulation (LES); namely to resolve the most energetic scales of the flow and model the effect of the unresolved scales on the resolved ones. The approach is justified and motivated by the universality of the small scales, as discussed in Section 4.1. In contrast to the RANS formulation, which is a model, LES is an

approximation of the Navier-Stokes solution of a given problem, being a step towards DNS.

In order to illustrate the LES concept, consider a generic transport equation,

$$\frac{\partial u}{\partial t} + \frac{\partial F(u,x)}{\partial x} = 0. \tag{4.9}$$

Since only the larger scales of the flow can be resolved, the higher frequency scales are simply filtered out. The filtering operations can be done in several ways, explicitly or implicitly, locally or globally. In many LES formulations, one does not filter the variables explicitly but rather work with the filtered equations directly. This may also be described as filtering by using the computational grid or implicit filtering.

When Equation 4.9 is filtered by applying a (linear) filtering operator on each term, the equation for the filtered variable takes on the form of Equation 4.10. The resulted outcome of the filtering is the elimination of the unresolved scales, regardless of whether an explicit or an implicit filtering is used.

$$\frac{\partial \overline{u}}{\partial t} + \frac{\partial \overline{F(\overline{u},x)}}{\partial x} = \frac{\partial \overline{F(\overline{u},x)}}{\partial x} - \frac{\partial F(u,x)}{\partial x} = \mathcal{G}. \tag{4.10}$$

The exact form of $\mathcal{G}$ is dependent on the applied filtering kernel and the filtering operation is assumed to commute with the differentiation. This assumption about commutativity, though correct in the differential form, may not be correct for the discrete counterpart. If the assumption is valid, $\mathcal{G}$ contains terms that stem from nonlinearities in the equation and expresses the effect of the unresolved scales on the resolved ones.

For the Navier-Stokes equations, the only contribution is due to the convective terms, which are non-linear. Their contributions are called the Sub-Grid Scale (SGS) terms and their effect on the resolved scales has to be accounted for. The resulting system of equations are closed with an SGS model and, given the appropriate boundary conditions, it can be solved numerically.

4.2.2a. *Subgrid scale modeling.* In the LES framework, the filtering operation generates the SGS terms in the equations, as described above. Due to the importance of the unresolved scales, many different approaches exist for capturing their effect on the resolved scales.

Generally speaking, the main role of the SGS term is to account for the effects of the small scales on the large ones and the flow in general. An obvious effect is the dissipation which takes place at the smallest scales of the flow. Thus, SGS terms (and SGS models) must be *dissipative*, which incidentally is also a requirement for stable numerical schemes. Another characteristic that one often associates with a SGS model is that it should have the ability

to intermittently transfer energy from small to large scales, to account for backscatter.

SGS models range from quite simple ones, aiming at dissipating energy at a correct rate to the more complex ones, of non-local and/or non-linear character. It is important to emphasize that the choice of a certain SGS model must be based on the physical characteristics of the problem and the ability of the model to account for important features of the specific problem. Thus, there are no generally valid SGS models since flows may differ largely from each other also in the small scale characteristics.

The simplest model in practice is the standard Smagorinsky model. This is a very commonly used SGS model which also serves as the origin of several more advanced models. The Smagorinsky model, Equation 4.11, is an analogy to the RANS variant of the eddy viscosity model.

$$\tau_{ij}^r = -2\nu_r \overline{S}_{ij}, \tag{4.11}$$

$$\nu_r = (C_s\Delta)^2\overline{\mathcal{S}}, \qquad \overline{\mathcal{S}} \equiv \left(2\overline{S}_{ij}\overline{S}_{ij}\right)^{1/2}. \tag{4.12}$$

In the Smagorinsky model, the SGS stress, (τ_{ij}^r), is related to the filtered rate of strain, $\overline{S}_{ij}$, as in Equation 4.12. The Smagorinsky constant, C_s, and the filter width, Δ, will affect the transfer of energy from the filtered scales to the residual motions.

In the case of the Smagorinsky model and any other eddy viscosity type of model, energy transfer is one-way from the filtered motions to the residual motions and there is thus no backscatter. This SGS model, probably the most widely used model, it is considered to be too dissipative in general and in particular at low Re, transitional, inhomogeneous flows (c.f. Pope (2000)). The Smagorinsky model states explicitly that the SGS term is of second order in terms of the filter width, or cutoff length, Δ. This implies that the error associated with the SGS model may be larger than the truncation errors. This may cause problems if simulating laminar and transitional flows.

Another issue related to SGS modeling is handling the near wall behavior. Here, the behavior of turbulence depends on the local and boundary conditions, being problem dependent and not universal. Due to this problem dependence of the turbulence properties of, no generally valid model has been formulated.

Other approaches that gained some popularity are the hybrid methods in which RANS models are used near the wall and LES is used elsewhere. The hybrid approach is rather straight forward from a conceptual point of view but it may be intricate to implement without causing obviously incorrect flow solutions. Additionally, there is no solid physical foundation for the hybrid approach since the near wall RANS handling is not generally valid and the

transfer of information in the LES-RANS interface invariably lead to a loss of information.

A significant improvement in the problematic areas of the Smagorinsky model is made by the dynamic approach (dynamic Smagorinsky model). In this model, the constant C_s is given a *local* value that is derived by assuming an asymptotic behavior of the SGS term as the filter size is reduced. The approach is done by using two filters of different sizes in order to make an estimation of the SGS behavior and thereby obtaining an optimal C_s value. The dynamic approach can handle fully resolved (laminar or low-Re) regions by computing the vanishing value of the coefficient. Also, if the assumption of asymptotic behavior is valid for any reason near the wall, the approach is still valid. The main difficulty that may be encountered is that the coefficient attains a negative value, which may lead to numerical instability. Olsson & Fuchs (1998) show that this issue can be circumvented by satisfying a total dissipative condition.

4.2.2b. *Implicit LES.* When the filtered Equation 4.10 is approximated by a discrete approximation its principal appearance is:

$$\frac{\partial \overline{u}}{\partial t} + \frac{\partial \overline{F(\overline{u}, x)}}{\partial x} = \frac{\partial \overline{F(\overline{u}, x)}}{\partial x} - \frac{\partial F(u, x)}{\partial x} = \mathcal{G} + T(\overline{u}, \Delta x, \Delta t). \tag{4.13}$$

In Equation 4.13, T is representing the truncation errors of the discretization scheme.

The role of the physical SGS and the contribution of the truncation errors are additive. In fact, if one does not have a clear distinction between the filter width and the numerical scale (i.e. these two scales vanish at the same rate), the effects of the SGS terms can hardly be distinguished from the effects of the discretization errors. This is so since, as the filter and numerical scales are reduced, the contribution of the SGS and the discretization error terms becomes arbitrarily small.

A general problem is that one has to express the effects of SGS in terms of the resolved scales and the loss of information (due to filtering) has to be recovered. It is not self-evident that such a deconvolution is possible at all without introducing a set of assumptions. Therefore, when explicit SGS models are used, some hypothesis or physical reasoning must be introduced in order to resolve this.

All the Large Eddy Simulation calculations performed in this work does not use an explicit subgrid scale model. This approach is usually called Implicit LES (ILES). With ILES, adequately fine grids are used so that the errors caused by approximating the SGS terms are of the order of the truncation errors (i.e. the right hand side of Equation 4.13). For this approach the inherent dissipation of the numerical schemes is used to account for the dissipative role of the SGS

term. For a comprehensive review of the approach itself and it's applicability to a variety of problems, see Grinstein *et al.* (2007); Garmann *et al.* (2012).

The advantages with this LES approach are simplicity and relatively lower computational cost as compared with a standard LES that includes explicitly SGS modeling. However, the dissipation of energy and any structural properties of the unresolved scales are completely dependent on the grid and on the numerical scheme (i.e. non-physical parameters), making the identification of the SGS effects difficult. For conventional LES using a dissipative SGS model such as the Smagorinsky model, it is essential that the numerical dissipation is as low as possible so that the small scale effects are left to the model. For LES without explicit SGS model (i.e. the so called "implicit" LES), the coupled nature of the SGS effects and the numerics requires that the spatial resolution is adequate.

Generally speaking, using explicit SGS models allows one to use somewhat coarser grids. Finally, one might argue that implicit LES is not true LES as it will converge to a DNS if the resolution is increased. Because of this, one cannot obtain (in implicit LES), in the strict sense, grid-independent solutions except in the DNS limit. If this property is important or not is largely a question of preference. The usability, applicability and accuracy of the implicit LES approach has been demonstrated in many occasions and for a large number of different flow cases, see e.g. Grinstein *et al.* (2007).

CHAPTER 5

Data analysis and post-processing techniques

In this chapter several techniques used for data reduction and analysis are presented.

5.1. Flow uniformity

Three-dimensional and unsteady turbulent flow fields in complex geometries, such the exhaust manifold of an internal combustion engine, are often not easily understood. However, there is often a need to represent the data from the flow field in a more low-dimensional way. In order to reduce the data, the flow uniformity index, γ is defined.

$$\gamma = 1 - \frac{1}{2\overline{q}A}\sum_{i=1}^{n}\sqrt{(q_i - \overline{q})^2}A_i \tag{5.1}$$

The plane in question is divided into n regions, each with a corresponding q_i which represent the investigated variable. The total area of the plane is A and $\overline{q}$ is the area weighted average of q. This method is used in this thesis as a way of representing the non-uniformity of the flow in a plane when q in the axial velocity component.

5.2. Power spectral density

The power spectra of various signals from the LES data are used in this thesis for several purposes. What is displayed in these figures is the power spectral density (PSD) of the data in question, defined as:

$$PSD(\omega) = \frac{\Delta^2}{T}\left|\sum_{n=1}^{N} x_n e^{-i\omega n}\right|^2 \tag{5.2}$$

The data x is a series of samples taken from a continuous process at N equidistant times, with a sampling frequency $1/\Delta$. The length of the time-series is $N * \Delta = T$ and the angular frequency is $\omega = 2\pi f$ with f being the frequency in Hz. The transform 5.2 is usually not evaluated directly, but computed by a fast Fourier transform algorithm (FFT) which greatly reduces computational time. Because of the non-harmonic, turbulent signals of finite length generated

by the LES, simply computing the PSD is likely to exhibit a large variance in the generated power spectrum. In order to increase the accuracy of the PSD, the Welch method is used to reduce the noise in all spectra of this thesis. The basic algorithm is as follows for the discrete and finite data series x:

1. x is divided into M segments which are of equal length and overlap by 50%.
2. Any data in x that can not be included in the M segments are not considered
3. Each segment is windowed by a Hamming window of equal length to the segment.
4. The PSD of the windowed segment is calculated using a fast Fourier transform
5. After repeating the steps 1-4 for the M segments, the average PSD over all segments is calculated.

When using the Welch algorithm, care must be taken when choosing the length of the signal segments. Perhaps trivially understood, the length of the segment will have a large effect on the computed spectra which, in turn, is dependent on the signal character. When dealing with signals that have important phenomena at widely separated frequencies, it may be very difficult to find a single window size that will clearly show all phenomena. In such situations it may be beneficial to compute several PSD with different segment lengths and combine their results.

Worth remembering is also that the interpretations of the PSD is very dependent on how it is presented. Spectra presented in log-log plots are not likely to be interpreted in the same way as when linear axes are used.

5.3. Correlation techniques

The cross-correlation is the similarity of two signals as a function of an applied time lag between them. There is no strict definition of cross-correlation and in some contexts, the designation cross-covariance is used instead. In this thesis, the correlation between two signals at locations of interest, the cross correlation of the signals $x(t)$ and $y(t)$ which are of length N is computed in the following way:

$$R_{xy}(m) = \begin{cases} \sum_{n=0}^{N-m-1} x(n+m)y^*(n) & m \geq 0 \\ R_{xy}(-m) & m < 0 \end{cases}, \tag{5.3}$$

The superscript $*$ here means complex conjugate which in the case of real signals is the same as the signal itself. The autocorrelation, R_{xx}, which is the similarity of a signal with itself as a function of an applied lag is simply Equation **??** where $x(t) = y(t)$.

The coherence function will estimate the correlation between signals $x(f)$ and $y(f)$ at the frequencies f.

$$C_{xy}(f) = \frac{|P_{xy}(f)|^2}{P_{xx}(f)P_{yy}(f)} \tag{5.4}$$

In Equation 5.4, $P_{xx}(f)$ is the power spectral density of $x(f)$, $P_{yy}(f)$ is the power spectral density of $y(f)$ and $P_{xy}(f)$ is the cross power spectral density of the signals $x(f)$ and $y(f)$.

5.4. Vortex detection

Vortical structures are important features in a variety of fluid flows, from turbulence to vortex shedding, wingtip vortices and tornadoes. This, coupled with the difficulty of mathematically defining a vortex has led to a large number of different approaches for identifying vortices in a three-dimensional flow field, see for example Hansen & Johnson (2004).

5.4.1. λ_2 *criterion*

The λ_2 criterion was proposed by Jeong & Hussain (1995) as a way of identifying vortex cores. It is based on that, at the vortex core, there is a local pressure minima. The method uses the velocity gradient decomposition,

$$\nabla \mathbf{u} = \mathbf{S} + \mathbf{\Omega}, \tag{5.5}$$

which is the sum of the rate of strain tensor,

$$\mathbf{S} = \frac{1}{2}\left[\nabla \mathbf{u} - (\nabla \mathbf{u})^T\right], \tag{5.6}$$

and the vorticity (rotation) tensor,

$$\mathbf{\Omega} = \frac{1}{2}\left[\nabla \mathbf{u} + (\nabla \mathbf{u})^T\right]. \tag{5.7}$$

Consider the incompressible and inviscid Navier-Stokes (momentum) equation in the following form:

$$\frac{D}{Dt}\mathbf{S} + \mathbf{S}^2 + \mathbf{\Omega}^2 = -\frac{1}{\rho}\nabla\left(\nabla p\right). \tag{5.8}$$

If the unsteady straining is negligible, the first term will be small and Equation 5.8 will simplify to:

$$\mathbf{S}^2 + \mathbf{\Omega}^2 = -\frac{1}{\rho}\nabla\left(\nabla p\right). \tag{5.9}$$

The left hand side of Equation 5.9 contain the rate of strain and vorticity tensors and the right hand side is made up of the Hessian of the pressure, $\nabla\left(\nabla p\right)$. If the pressure Hessian, which is a 3 by 3 matrix in all points of a three dimensional flow field, has two negative eigenvalues then that point will

be a local pressure minima. This in turn means that if the tensor on the left hand side has two positive eigenvalues, that point will be a pressure minima.

5.4.2. *Practical issues*

The λ_2 criterion can be used to find vortices in any flow field, including those that are unsteady, compressible and viscous. It is a Eulerian and local method so it can be used in unsteady flows without considering flow history or geometry. It is also Galilean invariant which means the the same vortices are detected regardless of which coordinate system is used, as long as the coordinate systems are stationary or moving with constant speed in relation to each other.

In practice, one computes the second eigenvalue of the left hand side of Equation 5.9 for each point of interest, and visualizes this scalar field as either iso-surfaces or as iso-contours on a plane. The main difficulties lie in choosing an appropriate numerical value for the visualization level and to discriminate the actual vortices from so-called *false positives*, i.e. regions of positive λ_2 that do not contain vortices.

5.5. Flow decomposition methods

In this thesis, two data-based flow decomposition methods are used: Proper orthogonal decomposition (POD) and Dynamic Mode Decomposition (DMD). The reasons for applying them are the complexity of the three-dimensional and unsteady flows considered and the difficulty of quantifying flow features. They are used to extract structures which are important from an energy sense (POD), but also structures linked to specific frequencies (DMD).

5.5.1. *Proper Orthogonal Decomposition*

5.5.1a. *Background.* Proper orthogonal decomposition, POD, is a particular method used to decompose a data set. Consider the following:

$$\mathbf{u}\left(\mathbf{x},t\right) \approx \sum_{j=1}^{J} a_j\left(t\right) \boldsymbol{\phi}_j\left(\mathbf{x}\right), \tag{5.10}$$

, where the time-dependent flow field $\mathbf{u}\left(\mathbf{x},t\right)$ is approximated by a finite sum of the functions $\boldsymbol{\phi}_j$ and $a_j\left(t\right)$. The functions $\boldsymbol{\phi}_j$ can be chosen in different ways and POD is simply the choice of $\boldsymbol{\phi}_j$ that produces the best approximation for any J of the function $\mathbf{u}\left(\mathbf{x},t\right)$ in a least-squares sense for orthonormal $\boldsymbol{\phi}_j$. In the fluid mechanics context, the method was first proposed by Lumley (1967).

POD is usually used to find a low-order approximation of a complex, high-dimensional system or field. If POD is applied to a time-dependent fluid field it can be used to extract the energetically important spatial modes and their

variation in time.

$$\mathbf{u}(\mathbf{x},t) = \underbrace{a_0\boldsymbol{\phi_0}(\mathbf{x})}_{\text{mean field}} + \underbrace{\sum_{j=1}^{J} a_j(t)\,\boldsymbol{\phi_j}(\mathbf{x})}_{\text{energetic}} + \underbrace{\sum_{j=J+1}^{\infty} a_j(t)\,\boldsymbol{\phi_j}(\mathbf{x})}_{\text{low energy}}, \tag{5.11}$$

This data can then be used to gain understanding of the modes, and therefore the flow itself, for example by showing coherent fluid motion which is usually energetic. This division assumes that there is a mean flow, which is not always the case in pulsating flows. Choosing J is of course completely subjective and several choices can be argued for. The only general statement that can be made is that, for fluid flow fields, most of the energy is usually found in a small portion of the computed modes.

5.5.1b. *POD algorithm.* For the practical implementations of the POD, the data is discrete and in the form of snapshots of the system state at (usually but not necessarily) regular intervals. All of the following assumes that the data are M snapshots from a time-dependent three dimensional fluid simulation with velocity $\mathbf{u} = (u, v, w)$ and that the number of grid points is N. To compute the POD, the data is collected in the matrix $\mathbf{X}$,

$$\mathbf{X} = \begin{bmatrix} u(\mathbf{x}_1,t_1) & \cdots & u(\mathbf{x}_1,t_M) \\ \vdots & \ddots & \vdots \\ u(\mathbf{x}_N,t_1) & \cdots & u(\mathbf{x}_N,t_M) \\ v(\mathbf{x}_1,t_1) & \cdots & v(\mathbf{x}_1,t_M) \\ \vdots & \ddots & \vdots \\ v(\mathbf{x}_N,t_1) & \cdots & v(\mathbf{x}_N,t_M) \\ w(\mathbf{x}_1,t_1) & \cdots & w(\mathbf{x}_1,t_M) \\ \vdots & \ddots & \vdots \\ w(\mathbf{x}_N,t_1) & \cdots & w(\mathbf{x}_N,t_M) \end{bmatrix}. \tag{5.12}$$

Clearly, this matrix will be of the size 3N by M. The POD method is then recast from a maximization problem to a eigenvalue problem,

$$\mathbf{X}\mathbf{X}^T\boldsymbol{\phi} = \boldsymbol{\lambda}\boldsymbol{\phi}, \tag{5.13}$$

, where the eigenvalues of the covariance matrix of $\mathbf{X}$, $\mathbf{X}\mathbf{X}^T$, $\boldsymbol{\lambda}_j$ correspond to the kinetic energy of the mode $\boldsymbol{\lambda}\boldsymbol{\phi}_j$, see Holmes *et al.* (1998). The difficulty in finding the eigenvalues of the covariance matrix will be dependent on the size of it and for LES data, N is typically very large. To address this difficulty, the so-called method of snapshots is used. Consider the singular value decomposition (SVD) of the matrix $\mathbf{X}$

$$\mathbf{X} = \mathbf{U}\boldsymbol{\Sigma}\mathbf{V}^T, \tag{5.14}$$

where the matrices $\mathbf{U}$ and $\mathbf{V}$ are orthonormal and $\mathbf{\Sigma}$ is a diagonal matrix. Following this, the autocorrelation matrix can be written as:

$$\mathbf{X}\mathbf{X}^T = \mathbf{U}\mathbf{\Sigma}\mathbf{V}^T \left(\mathbf{U}\mathbf{\Sigma}\mathbf{V}^T\right)^T. \tag{5.15}$$

Since for orthogonal matrices, $\mathbf{A}^T = \mathbf{A}^{-1}$ and for the matrix inverse $(\mathbf{AB})^{-1} = \mathbf{B}^{-1}\mathbf{A}^{-1}$, this can be rewritten,

$$\begin{aligned} \mathbf{X}\mathbf{X}^T &= \mathbf{U}\mathbf{\Sigma}\mathbf{V}^T\mathbf{V}\mathbf{\Sigma}^T\mathbf{U}^T \\ \mathbf{X}\mathbf{X}^T &= \mathbf{U}\mathbf{\Sigma}^2\mathbf{U}^T \\ \mathbf{X}\mathbf{X}^T\mathbf{U} &= \mathbf{U}\mathbf{\Sigma}^2, \end{aligned} \tag{5.16}$$

where the diagonal elements of $\mathbf{\Sigma}^2$ are the eigenvalues of the autocorrelation matrix and the columns of $\mathbf{U}$ contain the POD modes. The same procedure can be applied to the matrix $\mathbf{X}^T\mathbf{X}$,

$$\begin{aligned} \mathbf{X}^T\mathbf{X} &= \mathbf{V}\mathbf{\Sigma}^T\mathbf{U}^T\mathbf{U}\mathbf{\Sigma}\mathbf{V}^T \\ \mathbf{X}^T\mathbf{X} &= \mathbf{V}\mathbf{\Sigma}^2\mathbf{V}^T \\ \mathbf{X}^T\mathbf{X}\mathbf{V} &= \mathbf{V}\mathbf{\Sigma}^2. \end{aligned} \tag{5.17}$$

The singular values of $\mathbf{\Sigma}$ are the square root of the eigenvalues of both the covariance matrix, $\mathbf{X}\mathbf{X}^T$, and the smaller (for LES data) $\mathbf{X}^T\mathbf{X}$. This means that, instead of computing the SVD of the large matrix in order to obtain the modes and time-coefficients, we may use the smaller matrix.

$$\mathbf{U} = \mathbf{X}\mathbf{V}\mathbf{\Sigma}^{-1} = [\boldsymbol{\phi}_1 \cdots \boldsymbol{\phi}_M] \tag{5.18}$$

$$\mathbf{\Sigma}\mathbf{V}^T = \begin{bmatrix} a_1(t) \\ \vdots \\ a_M(t) \end{bmatrix} \tag{5.19}$$

POD decomposes to flow field based on energy and the spatial modes are orthogonal in space.

5.5.2. *Dynamic Mode Decomposition*

5.5.2a. *Background.* The purpose of flow field decomposition in the context of this thesis was also to gain insight into the three-dimensional and unsteady structures present in the flow. Thus, the Dynamic Mode Decomposition (DMD) is used (Schmid 2010; Rowley *et al.* 2009) to find the spatial shape of modes that are associated with certain (pre-computed) frequencies. The decomposition separates the spatial part of the flow structures from the time-dependent part in different ways depending on the purpose and the method. Consider a non-linear system $\mathbf{u}$ evolving in time like

$$\mathbf{u}_m = f(\mathbf{u}_{m-1}). \tag{5.20}$$

The linear Koopman operator, K, is defined as an operator that will move a function $g(\mathbf{u})$ forward in time like

$$Kg(\mathbf{u}_{m-1}) = g(\mathbf{u}_m) \tag{5.21}$$

The eigenvalues and eigenfunctions of the operator K will be called λ_i and $\xi_i(\mathbf{u_m})$, respectively.

$$K\xi_i(\mathbf{u}_m) = \lambda_i \xi_i(\mathbf{u}_m) \tag{5.22}$$

Consider a vector function of the initial velocity field $\mathbf{g}(\mathbf{u}_1)$, at discrete grid points in some domain. Provided that $\mathbf{u}$ lies within the space spanned by the eigenfunctions of K, one may expand $\mathbf{g}(\mathbf{u}_1)$ into a linear combination of eigenfunctions and the expansion coefficients $\mathbf{v}_j$ (Mezić 2005).

$$\mathbf{g}(\mathbf{u}_1) = \sum_{j=0}^{\infty} \xi_j(\mathbf{u}_1)\mathbf{v}_j. \tag{5.23}$$

Using the above definition for K, one obtain the expansion of $\mathbf{g}(\mathbf{u_m})$ at any time m.

$$\mathbf{g}(\mathbf{u}_m) = K^m \mathbf{g}(\mathbf{u}_1) = K^m \sum_{j=0}^{\infty} \xi_j(\mathbf{u}_1)\mathbf{v}_j = \sum_{j=0}^{\infty} \lambda_j^m \xi_j(\mathbf{u}_1)\mathbf{v}_j \tag{5.24}$$

Equation 5.24 means that if one forms the matrix

$$\mathbf{\Phi} = [\boldsymbol{\xi}_1(\mathbf{u_1})\mathbf{v_1} \quad \boldsymbol{\xi}_1(\mathbf{u_1})\mathbf{v_1} \quad \cdots], \tag{5.25}$$

and the Vandermonde matrix,

$$\mathbf{S} = \begin{bmatrix} 1 & \lambda_1 & \lambda_1^2 & \cdots \\ 1 & \lambda_2 & \lambda_2^2 & \cdots \\ \vdots & \vdots & \vdots & \ddots \end{bmatrix}, \tag{5.26}$$

we may represent the velocity fields $\mathbf{U}_\infty = [\mathbf{u}_1 \quad \mathbf{u}_2 \quad \cdots \quad \mathbf{u}_\infty]$ like this:

$$\mathbf{U}_\infty = \mathbf{\Phi S}. \tag{5.27}$$

The eigenvalues of the Koopman operator, K, will represent the development in time of the Koopman modes and together they describe the temporal evolution of system in question.

5.5.2b. *DMD algorithm.* First, assume that, for the velocity field $\mathbf{u}$ at time $k + 1$ is dependent on the field only at time k:

$$\mathbf{u}_{k+1} = \mathbf{A}\mathbf{u}_k. \tag{5.28}$$

In practical applications, we do not have an infinite number of velocity fields $\mathbf{U}_\infty$ to be represented by the Koopman modes and corresponding eigenvalues.

Rather, the velocity field is sampled at discrete instances with a certain frequency into so called snapshots $\mathbf{u}_i$. Now the $m-1$ first snapshots are used to express the m:th in the following way:

$$\mathbf{u}_{m+1} = \sum_{j=0}^{m} c_j \mathbf{u}_j + \mathbf{r}, \tag{5.29}$$

where the coefficients c_j are chosen so that $\mathbf{r}$ is minimized. Defining the snapshot, $\mathbf{U}$, and companion ,$\mathbf{S}$, matrix:

$$\mathbf{U}_1^m = [\mathbf{u}_1 \quad \cdots \quad \mathbf{u}_m] = \begin{bmatrix} u_{1,1} & \cdots & u_{1,m} \\ \vdots & \ddots & \vdots \\ u_{n,1} & \cdots & u_{m,n} \\ v_{1,1} & \cdots & v_{1,m} \\ \vdots & \ddots & \vdots \\ v_{n,1} & \cdots & v_{n,m} \\ w_{1,1} & \cdots & w_{1,m} \\ \vdots & \ddots & \vdots \\ w_{n,1} & \cdots & w_{n,m} \end{bmatrix},$$

$$\mathbf{S} = \begin{bmatrix} 0 & 0 & \cdots & 0 & c_1 \\ 1 & 0 & & 0 & c_2 \\ 0 & 1 & & 0 & c_3 \\ \vdots & & \ddots & & \vdots \\ 0 & 0 & \cdots & 1 & c_m \end{bmatrix} \tag{5.30}$$

where (u, v, w) are the velocity components in the (x, y, z) coordinate directions, n is the number of grid points and m is the number of snapshots. Using the above relations we can write

$$\mathbf{A}\mathbf{U}_1^m = \mathbf{U}_2^{m+1} = \mathbf{U}_1^m \mathbf{S} + \mathbf{r}\mathbf{e}, \qquad \mathbf{e} = [0 \quad \cdots \quad 1] \tag{5.31}$$

and compute the eigenvalues, λ_j, and eigenvectors, ψ_j, of $\mathbf{S}$ which are an approximation of the corresponding eigenvalues and eigenfunctions of $\mathbf{A}$. When this is done, the Koopman modes, which we will now call the DMD modes as they are an approximation of the Koopman modes, can be obtained by

$$\boldsymbol{\phi}_j = \mathbf{U}_1^m \boldsymbol{\psi}_j. \tag{5.32}$$

While is theoretically correct, computing the eigenvalues of the sparse companion matrix is not numerically robust due to the sensitivity to numerical noise. An alternative way to do the decomposition is to use singular value decomposition (SVD) of the snapshot matrix

$$\mathbf{U}_1^m = \mathbf{V}\boldsymbol{\Sigma}\mathbf{W}^T. \tag{5.33}$$

Using the SVD in Equation 5.31 yields:

$$\mathbf{V}^T\mathbf{A}\mathbf{V} = \mathbf{V}^T\mathbf{U}_2^{m+1}\mathbf{W}\mathbf{\Sigma}^{-1} \equiv \widetilde{\mathbf{S}}. \tag{5.34}$$

The matrix $\widetilde{\mathbf{S}}$ called the full companion matrix is a similarity transform of the companion matrix $\mathbf{S}$ which mean that they share eigenvalues and eigenvectors. To obtain the DMD modes with this approach do:

$$\boldsymbol{\phi}_j = \mathbf{V}\widetilde{\boldsymbol{\psi}}_j = \mathbf{U}_1^m\mathbf{W}\mathbf{\Sigma}^{-1}\widetilde{\boldsymbol{\psi}}_j, \tag{5.35}$$

where $\widetilde{\boldsymbol{\psi}}_j$ are the eigenvectors of the full companion matrix $\widetilde{\mathbf{S}}$. The frequency ω_j, and growth rate β_j of each mode can be obtained by:

$$\omega_j = \arctan\frac{\mathrm{Im}(\lambda_j)}{\mathrm{Re}(\lambda_j)}/\Delta t, \qquad \beta_j = \ln(\mathrm{mag}(\lambda_j))/\Delta t \tag{5.36}$$

5.5.3. *Practical issues and usage*

In practice, the flow decompositions mentioned here have issues that must be considered. Firstly, the methods process matrices which may come from a variety of sources. While they can be used to interpret fluid flow data, both DMD and POD are completely unaware of what fluid dynamics is. This means that the fluid dynamics knowledge must come from the user.

The geometrical distribution of the input data points have a meaning to the user which the methods are unaware of. For example, if the sample points lay on a circle which is a structure in itself, this will probably generate a circular structure in the resulting modes which is not necessarily a result of the flow dynamics.

Usually, at least when LES data is analyzed, it is also practically impossible (and usually undesirable) to do the decomposition on the entire flow field which typically has on the order of at least 10 million grid points. Therefore, the user has to decide where in the flow field the interesting and important dynamics take place.

This means that the user-controlled choice of points will affect the end result i.e. the appearance of the modes. Both the general location in the flow field and the distribution of the sample-points there will have an effect and, in order to take full advantage of the methods and avoid misinterpretations, thought must be given to this choice.

Typically, almost all of the energy in the POD is found in a very small number of modes. This gives that modes are built from fluid structures that can have very different dynamic behavior. If the flow considered has very clear dynamic behavior, for example vortex shedding from a cylinder, this is not an issue. However, for complex three-dimensional flows, the most energetic structures (modes) are not necessarily dynamically important.

DMD assumes that the fields can be decomposed into modes that have a set frequency and an exponential growth factor. If the flow has a tonal dynamics, this can be a good approximation even for relatively few snapshots. However, if the significant features are not tonal but broadband in nature, the method may not be able to capture the dynamics in a good way.

CHAPTER 6

Flows under consideration

6.1. Transonic channel

The computations were carried out in a model of a transonic wind tunnel set-up used by Sigfrids (2003), where the test section has a 0.12 m by 0.2 m cross section. On the floor of the wind tunnel, a half-airfoil bump with a cord of 0.19 m and a maximum height of 11 mm was placed, spanning over the entire width (z-direction) of the test section. The computational model of this tunnel geometry consists of a straight-walled channel with the same cross-section and bump shape as in Sigfrids (2003).This is shown in Figure 6.1. A number of parameter variations have been carried out and the corresponding computational cases are listed in Table 1.

6.1.1. *Computational mesh*

For all computed cases, structured grids are used. The meshes used for the bump cases are stretched in the x-direction at the inlet and outlet. This is done in order to reduce the reflection of pressure perturbations since they are not the subject of study and may adversely effect the numerical stability. In the bump mesh, stretching is used also in the wall normal direction using a stretch factor of 1.01.

6.2. Transonic flow in an model IC engine exhaust valve port

Simulations of the fluid flow in a model exhaust port, shown in Figure 6.2, has been carried out. This model has dimensions comparable to those in a normal passenger car engine. Only one valve lift has been investigated and all geometries and boundary conditions are steady in time, meaning no moving piston or valve. Three different cylinder (inlet) pressures have been considered, as stated in Table 2. The justification for the simplification of stationary geometry is that compared to the flow velocity in the exhaust port, the valve velocity is an order of magnitude less. The flow over the moving valve can then be viewed as several independent flows with different pressure ratios and valve lifts.

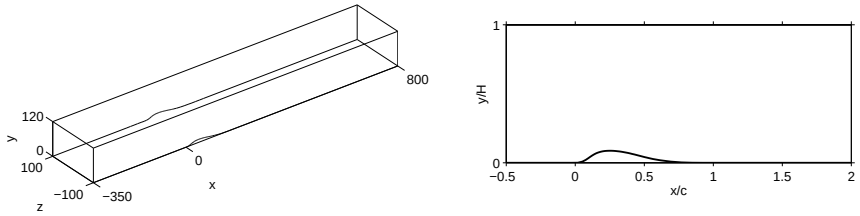

FIGURE 6.1. Computational geometry. Left: Isometric view [mm]. Right: spanwise cut of the region where interaction takes place [-].

Case nr	Grid size	Outlet BC	Other characteristics
1	3 M	steady 100 kPa	
2	3 M	steady 100 kPa	0.95 m domain length
3	3 M	steady 100 kPa	7.4 kg/s inlet mass flow
4	3 M	steady 100 kPa	Slot
5	3 M	steady 100 kPa	Power law
6	10 M	steady 100 kPa	
7	21 M	steady 100 kPa	
8	10 M	steady 92 kPa	
9	10 M	steady 96 kPa	
10	10 M	steady 104 kPa	
11	10 M	steady 108 kPa	
12	10 M	100 kPa mean 5 Hz	
13	10 M	100 kPa mean 10 Hz	
14	10 M	100 kPa mean 30 Hz	

TABLE 1. Computed cases overview. Misc column details deviations from the basic domain size (1.15 m length, 0.20 m width, 0.12 m height), inlet mass flow (7.3 kg/s), and inlet velocity profile (plug flow).

The boundary conditions are simplified for practical reasons, the correct *real* boundary conditions are not available for the geometry used and are not easily obtained. Actually, even if an actual engine geometry was used, the complete boundary conditions are not likely to be easily obtainable, if at all. If experimental data was available together with well documented experimental

FIGURE 6.2. Simplified exhaust valve geometry, cut at symmetry plane.

TABLE 2. Computed cases setup for simplified geometry

	$P_{tot,in}(Bar)$	$P_{stat,out}(Bar)$
Case 1	3	2
Case 2	40	10
Case 3	120	2

procedure, a much more physically accurate boundary description then what was used in this work is possible. Together with an actual geometry, it may then be possible to produce results with a more direct relevance to industrial geometries.

6.2.1. *Mesh*

For all computed cases, structured grids are used. The mesh used for the valve port cases are stretched at the inlet and outlet. This is done in order to reduce the reflection of pressure perturbations since they are not the subject of study and may adversely effect the numerical stability.

6.3. Heavy-duty exhaust manifold and port

The compressible flow calculations were carried out for two separate cases, the manifold and the exhaust port. Both the considered geometries are from the same Scania heavy-duty Diesel engine, the D12.

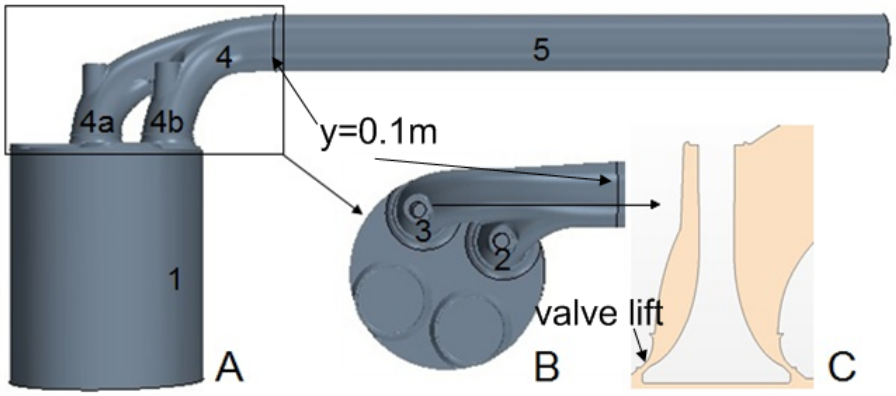

FIGURE 6.3. IC engine with only exhaust ports. A) The front view. B) The top view. C) The cross section of valve 3. 1) Cylinder. 2) Valve. 3) Valve. 4) Exhaust port. 5) Outlet domain.

6.3.1. *The exhaust port*

The exhaust port geometry consists of five distinct parts, a cylinder, a complex port where the two outlet from the cylinder are joined, two valves and a long exit pipe as shown in Figure 6.3. The exit pipe is 10 exhaust pipe diameters long. In the computational geometry of the port, the valves, valve seats and port itself are direct models of the actual engine parts. The rest of the port geometry is modeled after an experimental rig used to evaluate the pressure losses in the port.

6.3.2. *The exhaust manifold*

The geometry of the manifold is shown in Figure 6.4. Visible are the inlet to the turbine, in the negative z-direction, and to the EGR cooler. The cylinders will be referred to by the numbers 1 to 6 throughout this thesis and the numbering goes from 1 to 6 in the positive x-direction. When referring to the pipes of the manifold, the word runner will be used so that runner 1 means the pipe connected to cylinder 1, runner 1+2 the piping connecting cylinders 1 and 2 to the manifold and so on. Clearly visible in Figure 6.4 is the asymmetry of this manifold. Runners 1+2 and 5+6 are mirror images but the central part with runners 3 and 4 as well as the two outlets do not have a symmetry plane.

6.3.2a. *Exhaust port boundary conditions.* The boundary conditions are chosen to match those of the experimental investigation carried out using the same geometry. The inlet has a constant mass flow of 0.08 kg/s through the bottom of the cylinder liner. The two valves are fixed at 4 mm valve lift for all calculations

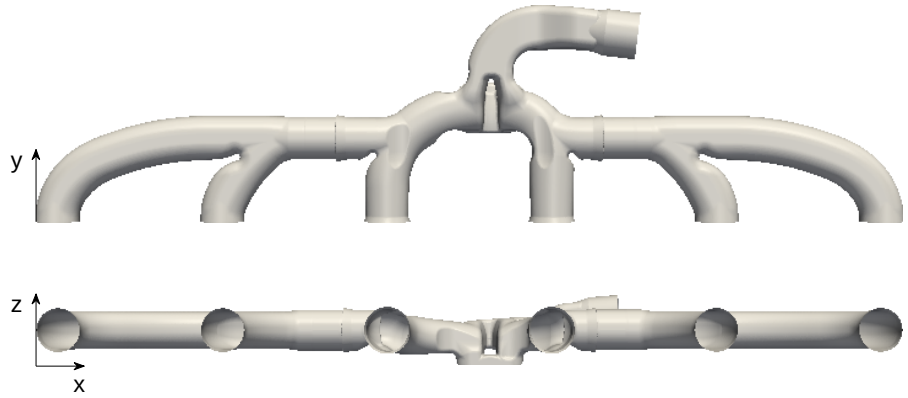

FIGURE 6.4. Manifold geometry and reference coordinate directions. Cylinders are numbered from the left.

TABLE 3. Manifold case description

Case	BC type	Inlet mass flow (mean, max) [kg/s]	Inlet temp (mean, max) [K]	Grid
M1	Steady	0.2, -	790, -	1
M2	Steady	0.2, -	790, -	2
M3	Steady	0.2, -	790, -	3
M4	1900 rpm	0.11, 0.48	786, 978	3
M5	1200 rpm	0.11, 0.48	786, 978	3

in this thesis. The outlet has a constant static pressure of 100 kPa and the wall boundary conditions are assumed to be no-slip velocity and adiabatic walls.

6.3.2b. *Manifold boundary conditions.* The boundary conditions of computational cases are detailed in Table 3. Boundary conditions are of two categories: Engine-like pulsating flow and steady flow trough one inlet runner. As the name implies, engine-like conditions are obtained from a low-order calibrated model of the actual engine. An example of the inlet condition for the engine-like cases can be seen in Figure 6.5.

The major mass flow pulses such as the one located at 120° are the sum of the blowdown pulse from one side of the manifold, which for this example is runner 2, and the scavenging pulse from the other side, from runner 6. The blowdown pulse has a double-peaked appearance, probably because of pulse interaction in the manifold. The second pulse in the total mass flow, for example located at 140° are caused by the second peak in the scavenging

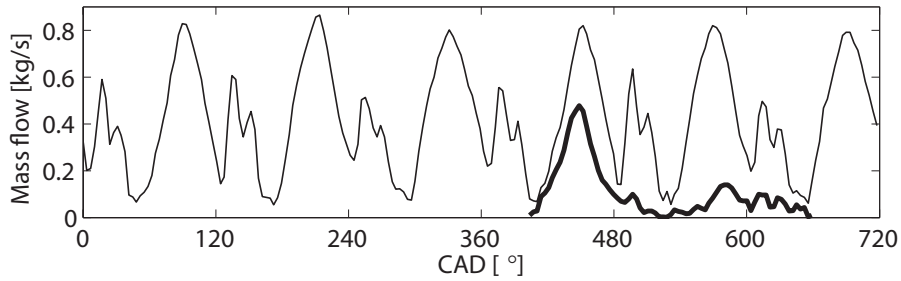

FIGURE 6.5. Phase averaged inlet mass flow from Case 4. '–' (thick line), mass flow from runner 1, '–' (thin line), mass flow from all runners.

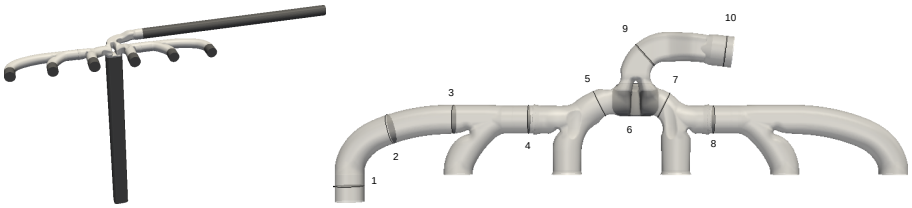

FIGURE 6.6. Left: Added volumes for computational stability in dark grey. Right: Manifold sample planes with corresponding numbers.

pulse. If the scavenging pulse did not have two peaks, the total mass flow would probably not display two distinct peaks, but rather have only one.

In reality, the manifold and the ports are constructed from cast iron, a material which is non-smooth. The main effects of surface roughness are related to the increased mixing introduced by the roughness and are: Increased flow losses, laminar/turbulent transition and flow separation delay. These effects are not unimportant but, for the not fully developed conditions in the manifold they are difficult to take into account. In fully developed flow conditions where the velocity profiles close to the wall are known, it is plausible to model the effect of wall roughness within LES but with the present case, one would need to resolve the roughness and this is not possible due to the associated computational cost.

Because of this, the wall boundary conditions are no-slip walls, as for a smooth boundary with either adiabatic or isothermal condition, depending on the case. For numerical stability, the actual inlet and outlet boundaries are placed at extended location (shown in Figure 6.6), in order to reduce the uncertainty in boundary condition. In these added regions, because their purpose is strictly numerical, the slip boundary condition is applied at the walls.

6.3.3. *Computational grids*

In the exhaust port, the grid is completely hexahedral. Cell size and shape varies throughout the computational domain. In the valve gap, the cells are highly isotropic with a 0.07 mm side which, compared to the valve lift (4 mm), implies that the relative cell size is $0.07/4 = 0.0175$. In the rest of the domain, and particularly in the outlet domain, (e.g. Part 5 in Figure 6.3) the grid is stretched in the flow direction.

For the exhaust manifold, the grids used are mostly isotropic with hexahedral cells and some polyhedra close to the walls. No grid stretching was used in the manifold domain (light gray in Figure 6.6). Quite aggressive grid stretching was used in the two outlet domains (dark gray in Figure 6.6) in order to damp the reflections from the outlets. Three different grid resolutions were used during the investigation, called grid 1, 2 and 3 with a cell size of 1, 0.8 and 0.6 mm respectively. These cell sizes correspond to a relative cell size of 0.023, 0.019 and 0.014 respectively when the diameter of the circular inlets to the manifold (43 mm) is used as reference.

6.4. Computational aspects

For all the work presented here, two general purpose, compressible flow, finite volume CFD code was used, EDGE (Eliasson 2001) and StarCCM+ (CD-Adapco 2011). The finite volume method is a discretization approach which is particularly suited to simulations where the flux is important, such as fluid mechanics. There are other approaches, such as the finite element method, which is widely used in solid mechanics for example. This section will briefly introduce the method for convection-diffusion problems such as the Navier-Stokes equations, for details the reader should consult e.g. Versteeg & Malalasekera (2007) Consider for the following sections, the governing equations presented in Chapter 3 written in the following form:

$$\frac{\partial}{\partial t}\left(B\right) + \frac{\partial}{\partial x_i}\left(F_I\right) + \frac{\partial}{\partial x_i}\left(F_V\right) = C, \tag{6.1}$$

where,

$$B = \begin{bmatrix} \rho \\ \rho u_1 \\ \rho u_2 \\ \rho u_3 \\ \rho h_0 - p \end{bmatrix}, \tag{6.2}$$

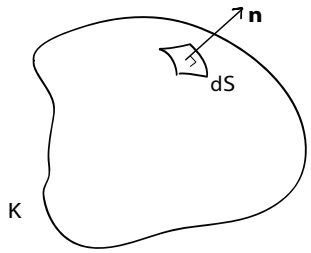

FIGURE 6.7. The finite volume potato. The volume K has the surface S, dS is a piece of S and has the normal vector **n** of unit length, pointing outwards.

the fluxes are split into inviscid (convective) and viscous (diffusive) parts,

$$F_I = \begin{bmatrix} \rho u_i \\ p\delta_{1i} + \rho u_1 u_i \\ p\delta_{2i} + \rho u_2 u_i \\ p\delta_{3i} + \rho u_3 u_i \\ \rho h_0 u_i \end{bmatrix}, \quad F_V = \begin{bmatrix} 0 \\ \tau_{i1} \\ \tau_{i2} \\ \tau_{i3} \\ -q_i - u_j \tau_{ij} \end{bmatrix}, \tag{6.3}$$

and C is the vector of source terms. Equation 6.1 is formulated for a fluid particle and given in *differential* form. However, in the computational implementation of these equations, the *conservation* form is used and for this, consider the arbitrary volume K in Figure 6.4, , it has the surface element dS which in turn has the normal vector **n**. Reformulating 6.1 to conservation form in the volume K gives:

$$\int_K \frac{\partial}{\partial t}(B)\, dK + \int_S (n_i F_I)\, dS + + \int_S (n_i F_V)\, dS = \int_K (C)\, dK. \tag{6.4}$$

6.4.1. *Spatial discretization in EDGE*

When the equations has been written in conservative form as in Equation 6.4, one may proceed to the discrete form for implementation in a flow solver. For this exercise, consider the control volume V_0. This figure is two-dimensional for clarity, all the following is however valid for three-dimensional volumes. The discrete form of Equation 6.4 is formulated as:

$$\frac{\partial}{\partial t}(B_0) + \sum_{k=1}^{N} F_{I,0k} n_{i,0k} S_{0k} + \sum_{k=1}^{N} F_{V,0k} n_{i,0k} S_{0k} = C_0 V_0, \tag{6.5}$$

where the subscript 0 refer to the control volume and N is the number of neighbor nodes (boundary surfaces) which for the control volume V_0 is 4. The flux vectors $F_{I,0k}$ and $F_{V,0k}$ are calculated on the connecting line between nodes 0 and k in different ways depending on the type of flux.

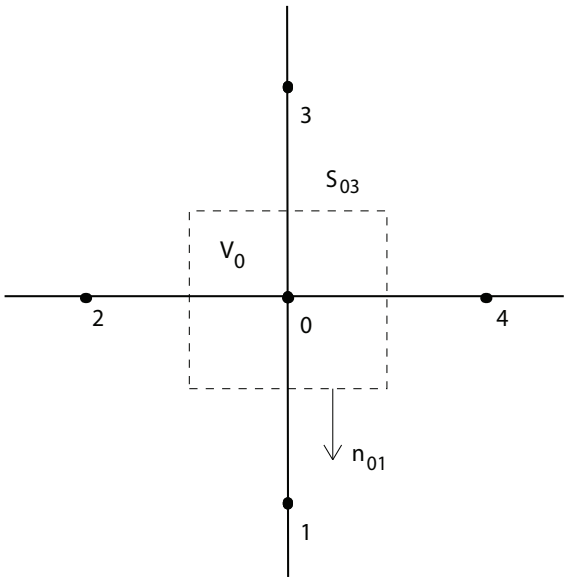

FIGURE 6.8. Control volume V_0. The volume is enclosed by the surfaces S_{0k}, k=1..4 and each surface has the normal vector, of unit length, n_{0k}, pointing outwards.

6.4.1a. *Inviscid flux.* In EDGE, the inviscid flux is handled by a formally second order central differencing scheme with added Jameson-type artificial dissipation, see Jameson *et al.* (1981). The reason for using a second order central scheme is the need to resolve sharp gradients (like shocks) while keeping computational effort reasonable on unstructured grids. In a convection-dominated flow such as the ones considered in this thesis however, the second order central differencing scheme alone causes unphysical oscillations and unbounded solutions. The problems manifest in regions with large pressure gradients, such as near shocks or stagnation points but also in smooth regions, where odd-even decoupling causes unphysical high-frequency oscillations. The solution to this problem is to introduce some way of dampening these unphysical oscillations, preferably without removing physical sharp gradients and oscillations. In EDGE the inviscid flux vector between the nodes 0 and 1 is calculated as

$$F_{I,01} = F_I\left(\frac{B_0 + B_1}{2}\right) - d_{01}, \tag{6.6}$$

where d_{01} is the artificial dissipation formulated as

$$d_{01} = \left(\varepsilon_{01}^{(2)}\left(B_1 - B_0\right) - \varepsilon_{01}^{(4)}\left(\nabla^2 B_1 - \nabla^2 B_0\right)\right)\phi_{01}\lambda_{01}. \tag{6.7}$$

The symbol ∇^2 here denotes the Laplacian operator,

$$\nabla^2 B_0 = \sum_{k=1}^{N} (B_k - B_0) = -NB_0 + \sum_{k=1}^{N} B_k, \tag{6.8}$$

and λ_{01} is the local spectral radius, defined as

$$\lambda_{01} = \left(|u_{i,01} n_{i,01}| + c_{01}\right), \tag{6.9}$$

where $u_{i,01} = (u_{i,0} + u_{i,1})/2$ and $c_0 1 = (c_0 + c_1)/2$ are the cell face speed and cell face speed of sound, respectively. The factor ϕ_{01} is used to allow the artificial dissipation to be dependent on grid stretching, it is formulated as

$$\phi_{01} = 4\frac{\phi_0 \phi_1}{\phi_0 + \phi_1}, \tag{6.10}$$

where

$$\phi_0 = \left(\frac{\lambda_0}{4\lambda_{01}}\right)^{\xi}, \tag{6.11}$$

and

$$\lambda_0 = \sum_{k=0}^{N} \left(u_{i,0k} n_{i,0k} + c_{0k}\right) S_k = \sum_{k=1}^{N} \lambda_{0k}. \tag{6.12}$$

where the factor ξ is set as 0.3. To put it very simply, the factor ϕ_{01} will increase the artificial dissipation in the direction normal to the stretching direction while in the stretching direction, it will be proportional to the local spectral radius. The second order difference dissipation function $\varepsilon_{01}^{(2)}$ is dependent on the pressure gradient and is intended to be active near shocks and small in regions of the flow where no shocks are present.

$$\varepsilon_{01}^{(2)} = \kappa^{(2)} \left(\left| \sum_{k=1}^{N} (p_k - p_0) \right| \Big/ \sum_{k=1}^{N} (p_k + p_0) \right) s_2 \tag{6.13}$$

The coefficient $\kappa^{(2)}$ is a tunable parameter, in the present simulations it is set to 0.5, and s_2 is a scaling factor set to

$$s_2 = \frac{3(N_0 + N_1)}{N_0 N_1}, \tag{6.14}$$

which is used to reduce the dependence of $\varepsilon_{01}^{(2)}$ on the number of cell neighbors. The function $\varepsilon_{01}^{(4)}$ is, in opposite to $\varepsilon_{01}^{(2)}$, intended to be switched off near shocks. It is defined as

$$\varepsilon_{01}^{(4)} = max(0, \kappa^{(4)} - \varepsilon_{01}^{(2)}) s_4, \tag{6.15}$$

where $\kappa^{(4)}$ is a tuning parameter like $\kappa^{(2)}$ which in the present simulations was set to 0.02 and s_4 is defined with s_2 like

$$s_4 = \frac{s_2^2}{4}. \tag{6.16}$$

To summarize, a formally second order central differencing scheme is used to discretize the convective, or inviscid, flux. To remove unphysical oscillations, artificial dissipation by second-, and fourth-order difference dissipation functions $\varepsilon_{01}^{(2)}$ and $\varepsilon_{01}^{(4)}$ are added.

6.4.1b. *Viscous fluxes.* Numerical treatment of the viscous, or diffusive, fluxes is more straight forward compared to the inviscid, or convective, fluxes. The diffusive flux terms are essentially made up by Laplacians and gradients of the dependent variables. In the EDGE code, the gradient of the dependent variable B_0 in the viscous flux is approximated as

$$\Delta B_0 \approx \frac{1}{V_0} \sum_{k=1}^{N} S_{0k} \frac{B_k - B_0}{|x_k - x_0|}, \tag{6.17}$$

where the denominator contain the distance between node 0 and k. The Laplacian of the dependent variable B_0 is approximated as

$$\nabla B_0 \approx \frac{1}{V_0} \int_{\partial V_0} B_0 n_{i,0k} dS = \sum_{k=1}^{N} \frac{1}{2} \left(B_0 + B_k\right) n_{i,0k} S_{0k}. \tag{6.18}$$

6.4.2. *Temporal discretization in EDGE*

Advancing the flow equations in time can be done in several ways but in principle the process is either implicit or explicit.

When employing implicit time stepping, a steady state-like iterative procedure is performed in each time step allowing larger time steps than numerical stability would allow in the case of explicit time stepping. This may greatly reduce computational time for some problems, when compared to explicit time stepping, and is the most generally applicable approach of the two.

Explicit time stepping uses a Runge-Kutta-type procedure to directly advance the flow equations in time making each time step much cheaper with regard to computational time compared to implicit time stepping. Additionally, explicit methods lend themselves more easily to parallel computation. However, as the length of the time step is directly linked to numerical stability it may require small time steps. In LES, for physical reasons, one uses time steps such that the fluid particles do not move more than one cell in a time-step. This might lead to, when the computational grid varies largely, that one could end up using very small time steps.

For the time discretization, consider Equation 6.1 written as

$$\frac{d}{dt}\left(B\right) = RHS, \tag{6.19}$$

with all the terms exept the time derivative collected in the RHS term. An explicit, q-stage, Runge-Kutta scheme for advancing Equation 6.19 from time

t=n to t=n+1 is written

$$\begin{aligned} B^1 &= u^n + \alpha_1 \Delta t (\mathrm{RHS})^n \\ B^2 &= u^n + \alpha_2 \Delta t (\mathrm{RHS})^1 \\ \vdots &\ \vdots\ \vdots \\ B^q &= u^n + \alpha_q \Delta t (\mathrm{RHS})^{q-1} \\ B^{n+1} &= B^q \end{aligned} \tag{6.20}$$

In the computations using EDGE performed in this work, explicit time stepping using a three-stage Runge-Kutta scheme of formally first order accuracy is used in Papers 1-3. In Papers 4-6, a four-stage second order Runge-Kutta scheme was used. The time step length was constant and chosen so that a maximum (acoustic) Courant number of around 0.6 was attained.

The coefficients α_n were set to

$$\alpha_1 = \frac{2}{3}, \quad \alpha_2 = \frac{2}{3}, \quad \alpha_3 = 1, \tag{6.21}$$

and

$$\alpha_1 = \frac{1}{4}, \quad \alpha_2 = \frac{1}{3}, \quad \alpha_3 = \frac{1}{2}, \quad \alpha_4, = 1, \tag{6.22}$$

for the two Runge-Kutta schemes respectively.

First order formal temporal accuracy may seem rather poor but, the total accuracy of the method depends on a combination of spatial and temporal discretization of the model. For the calculations performed, time steps are smaller by about three orders of magnitude when compared to the spatial steps and the spatial discretization is in fact the most significant for the total accuracy. The advantage of using a lower-order scheme is a reduction in computational time due to a decrease in the number of iterative stages.

The impact of using the four-stage method in place of the three-stage was found to be small however, so the decision was made to make the switch. No detailed investigation on the practical differences between the two discretization schemes were made.

6.4.3. *Discretization in StarCCM+*

As the majority of the results in this thesis are produced by using the EDGE code, StarCCM+ will only be described very briefly. StarCCM+ is a finite volume compressible flow solver that uses second order implicit time-stepping for both LES and URANS calculations. The inviscid fluxes (convective terms of the Navier-Stokes equations) were discretized by a bounded central-difference (BSD) scheme in the LES calculations. This BSD scheme can be generally described as a scheme mixing a first-order upwind scheme, a second-order upwind scheme and a central-differencing scheme. In the URANS calculations,

a second order upwind scheme was used to discretize the inviscid fluxes. The viscous fluxes were handled by second order central schemes for all StarCCM+ calculations.

6.4.4. *Boundary conditions in EDGE*

For the in-, and outflow boundaries, physics dictates by the theory of characteristics the amount of information that is allowed to be specified. More precisely, the amount of in-going characteristics at each boundary determines the number of required boundary conditions. At a subsonic inlet boundary, four conditions have to be given. At a supersonic inlet five conditions have to be given. At a subsonic or supersonic outflow one and no boundary conditions, respectively, are specified.

6.4.4a. *Inflow boundary conditions.* For the calculations presented in Papers 1-3 and Paper 5, a constant inlet mass flow is used. The basic boundary condition uses the desired mass flow together with a total temperature and flow direction to set a total pressure and temperature together with a flow direction at the flow inlet. Let the desired mass flow be $\dot{m}_r$, using the density ρ which in extrapolated upstream from the computational domain, and the cross-sectional area A, the inlet-normal velocity is calculated

$$u_n = \frac{\dot{m}_r}{\rho A}. \tag{6.23}$$

Using this velocity and the temperature, T, the Mach number is calculated $M = u_n/c$ and finally, the total pressure is calculated by the isentropic relation,

$$p_0 = p\left(1 + \frac{\gamma - 1}{2}M^2\right)^{\frac{\gamma}{\gamma-1}} \tag{6.24}$$

For paper 4 and 6, a varying inlet condition was specified by tabulated values of total pressure, total temperature and flow direction. None of the inlet boundary conditions permit outflow through the inlet boundary. If the pressure gradient across the inlet boundary is such that flow would be directed outwards, the boundary-normal velocity is set to zero.

6.4.4b. *Outlet boundary condition.* For all calculations performed, a constant static pressure was set at the outlet boundary. For some of the computations, this pressure was set as a function of time but this is in essence the same boundary condition. Using a constant pressure lead to an open-ended behavior with respect to reflections of pressure pulses which may cause problems. One solution to this is to use a so-called non-reflective outlet boundary condition which may remove, or at least reduce the reflected pressure pulses. For the calculations in this thesis, added elongated outlet domains with aggressive streamwise grid stretching was used instead to dissipate the pressure pulses.

The big advantage of this approach is simplicity and that it will dissipate high-frequency disturbances well. For low frequency disturbances, it may not be possible to increase the physical size of the outlet region enough to introduce enough dissipation.

6.4.5. *Assessment of numerical accuracy in EDGE*

Determining the numerical accuracy of the code and comparing results obtained by computations to experimental results are two ways of evaluating the validity of the computational results. While the investigation of numerical accuracy is fairly straightforward, comparisons of numerical and experimental results can be surprisingly difficult.

The problem is not in the actual comparison, but rather in addressing the same problem. Difficulty arises from the fact that experiments and simulations seldom have the same boundary conditions, both in terms of the domain geometry and, more often, in terms of the flow conditions at the inflow and outflow boundaries.

The literature contains a large number of experimental data but only very few of these include a detailed description of the set-up so as to allow one to set boundary conditions that are accurate enough (in terms of mean and turbulent quantities). The situation is even more problematic for LES, where one need instantaneous data at the boundaries.

With this background it is obvious that if one wants to make a side-by-side comparison of simulations and experiments then, aside from correctly describing the physics involved, one must put a considerable effort into making sure the boundary conditions match each other if close agreement is to be expected.

In order to determine the validity of the present work, the numerical accuracy of the code has been evaluated for the bump case by a method proposed by Celik (2005) and qualitative results were are compared to experimental results by Bron (2003) and Sigfrids (2003).

Due to both the difficulty in accurately reproducing the inlet and outlet conditions of the experiments and the apparent insensitivity of the main flow features to the incoming boundary layer, it was decided that simplified boundary conditions could be used. These consist, as stated in the above section, of a constant mass-flow inlet with a plug inlet profile and a constant static pressure outlet.

The main flow features are well captured by the simulation despite these simplifications while the exact shock position and other quantitative results are not. Since the motivation for the bump simulations was not to validate the experimental results but rather to investigate the code capabilities regarding

transonic flow and enhance the understanding of the sensitivity of the flow, the used boundary conditions are adequate.

The numerical accuracy study of the code resulted in an apparent accuracy of the order of 1.98, a result which must be considered very good with a formally second order spatial discretization. In this investigation, a first-order temporal discretization was used and the obtained results enforce that the total accuracy is indeed mostly determined by the spatial discretization for this case. We conclude by stating that the ability of the overall method to accurately handle transonic flow seem to be good.

CHAPTER 7

Results and discussion

In this chapter, selected results from Papers 1-6 are presented to give an overview of the work performed. Please consult Chapters 3, 2 and 6 for background and case descriptions.

7.1. Transonic channel flow

The transonic flow in a rectangular cross-section channel with a bump (see Figure 6.1) was realized for several different pressure rations. Qualitative investigations of the flow field in the tunnel confirm the occurrence of several expected phenomena observed in the experimental investigations by Bron (2003) and Sigfrids (2003). Under all conditions tested, a shock system is formed in the channel as well as a significant separation of the boundary layer downstream of the shock system. The shock system and separation appearance varies considerably in the range of pressure ratios tested, examples of the instantaneous and mean flow field at several different outlet pressures are shown in Figure 7.1.

Upstream of the bump, the developing boundary layer is very thin and is further compressed on the bump upstream of the shock. Downstream of the separation reattachment point, the flow has subsonic velocity and there are rapidly growing boundary layers on the walls. Depending on the tunnel pressure ratio, the shock is either regularly reflected, Mach reflected or not reflected in the tunnel ceiling.

The shock system and flow field downstream of the shock is unsteady in all the tested conditions. This basic unsteadiness is self-sustaining i.e. is not forced by varying boundary conditions and consist of several components. Of special interest is the low frequency streamwise oscillation of the entire shock system. In Figure 7.2 an example of the characteristic frequencies of the unsteadiness is presented as the normalized frequency multiplied power spectral density (see Chapter 5) as a function of dimensionless frequency, the Strouhal number.

$$\begin{aligned} St_L &= f^* L/U_0 \\ St_R &= f^* L/U_R \end{aligned}$$

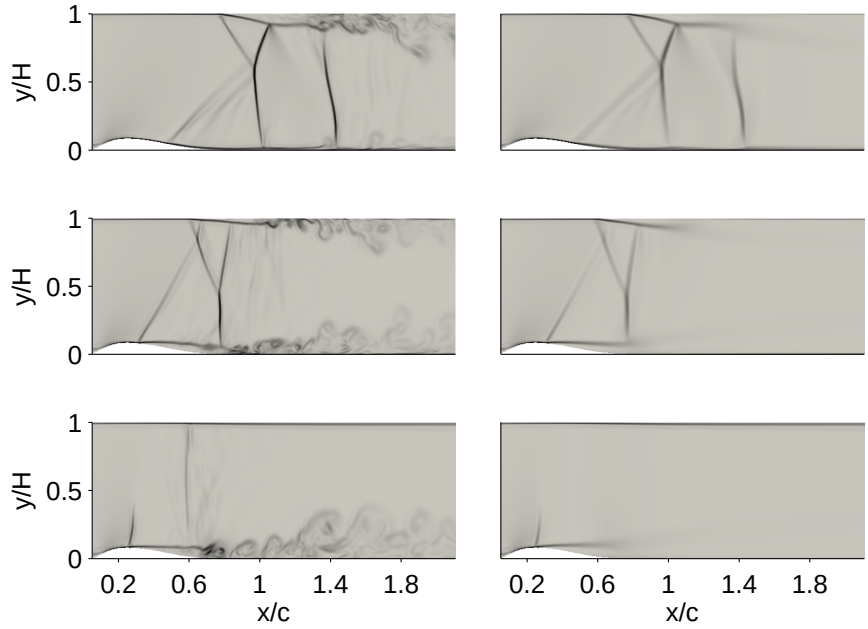

FIGURE 7.1. Mean (right) and instantaneous (left) normalized density gradient magnitude from spanwise cutplane at z=0. Outlet pressures, from top to bottom: 96 kPa, 100 kPa and 104 kPa

In these Strouhal numbers, f^* is an arbitrary frequency, L is mean separation length, U_0 is the mean free stream velocity upstream of the bump and U_R is the maximum mean recirculation velocity. These particular Strouhal numbers have been proposed previously in the literature by Wu & Martín (2007); Dussauge *et al.* (2006) as characteristic for the low-frequency, large scale unsteadiness of the shock system in shock/boundary-layer interaction (SBLI). In good agreement with Wu & Martín (2007) a characteristic shock frequency of $St_R \approx 0.8$ is found at both roof and floor. A more common scaling used in SBLI, St_L, yield results of $St_L \approx 0.25$ for the shock feet. This is an order of magnitude higher than the typical values found by Dussauge *et al.* (2006).

The range of St_L between 0.025 and 0.05 was suggested by Dussauge *et al.* (2006) to be characteristic for the low-frequency motion of the entire shock. The simultaneous movement of the entire shock, here characterized by the two shock feet in the roof and floor of the channel, was quantified by the coherence function (see Chapter 5). The coherence function basically gives the correlation

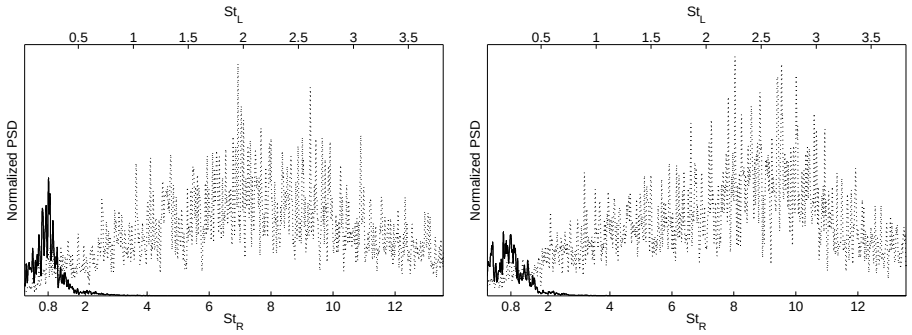

(a) Floor (b) Roof

FIGURE 7.2. Normalized PSD of pressure vs. dimensionless frequency for 100 kPa outlet pressure (Case 6, see Chapter 6). '—', mean location of the shock foot; '· · · ' , mean reattachment position.

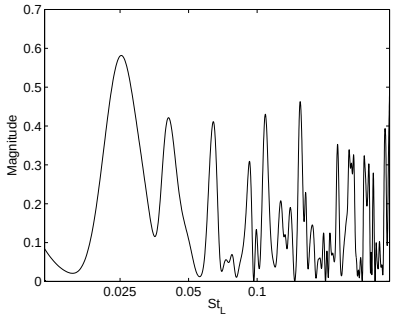

FIGURE 7.3. Coherence function (see Chapter 5) of pressure fluctuations at roof and floor shock feet for Case 6 (see Chapter 6)

of two signals as a function of frequency and the result of computing this for the pressure fluctuations at roof and floor shock feet is shown in Figure 7.3.

The coherence function show a clear correlation at St_L around 0.025 which is within the range suggested by Dussauge *et al.* (2006). Finding this Strouhal number shows that the characteristic low-frequency dynamics are present and that they involve the entire shock system.

There are several possible driving mechanisms for the unforced shock system unsteadiness with the most likely being either acoustic interaction via a

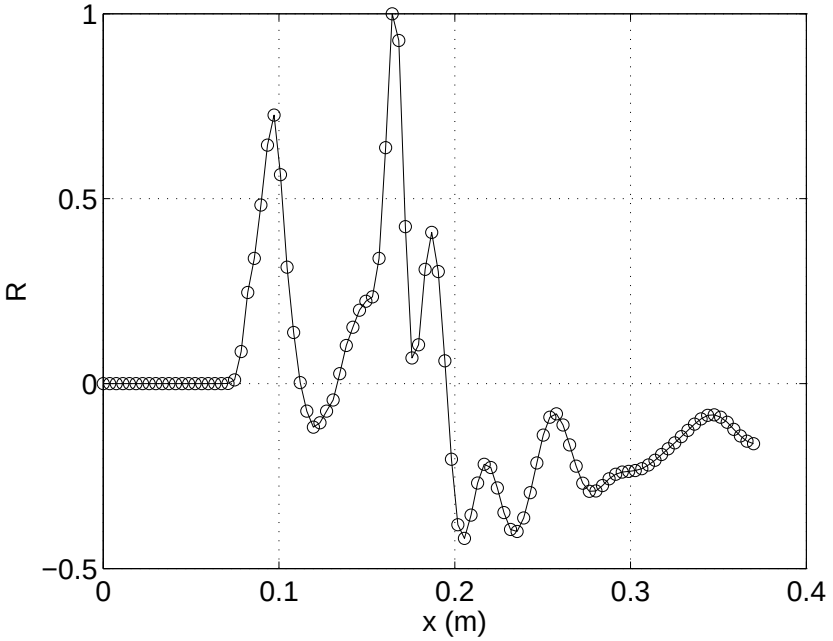

FIGURE 7.4. Spatial correlation of the streamwise velocity fluctuations along a line above the bump surface.

standing wave in the downstream part of the domain or that the unsteady separation bubble is responsible.

In order to investigate the interaction of the shock and the separated boundary layer, monitoring points at regular intervals along a line 6 mm from the top of the peak bump surface were used. One of these points, called x_r located in the separation bubble shear layer, was used as basis for cross correlations (see Equation 5.3) of the streamwise velocity fluctuations with all other points along the line. In this particular usage of Equation 5.3, the functions under consideration are dependent on both time and space and so at each location one value of the correlation function was attained. The results are plotted in Figure 7.4 where x_r is the point having $R = 1$ as it is completely correlated with itself and this is used as a normalization of R.

The peak having $R \approx 0.72$ is the physical location of the separation and shock foot, x_s. This result shows a strong spatial correlation between x_r and x_s implying that the unsteady motion of the shock foot and the separated boundary layer are strongly related.

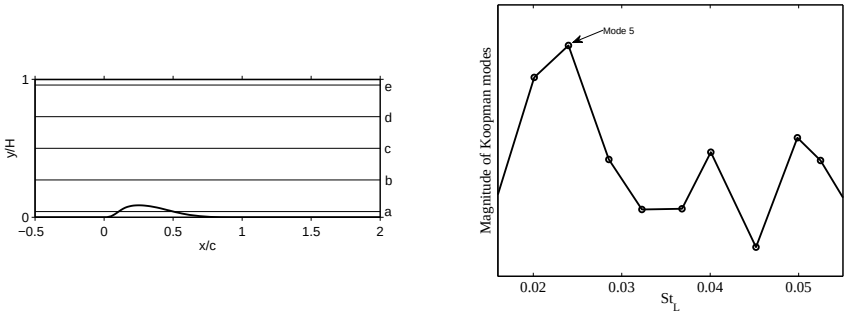

(a) Visualization planes

(b) DMD mode spectra

FIGURE 7.5. (a) The visualization planes used in Figure 7.6. (b) Spectra for the DMD modes. Magnitude of the mode j is the L_2 norm of $\boldsymbol{\phi}_j$ in Equation 7.1

No evidence of the acoustic modes directly affecting the shock dynamics as mentioned by for example Sajben *et al.* (1984) could be found during this work. However, the behavior of the shock at high outlet pressures when the flow is not choked is significantly more unsteady as compared to the choked flow case. Acoustic modes are believed to be present in the channel at all outlet pressures, but when the flow is choked the disturbances emanating from the boundary layer dominate these and are the primary force behind the shock motion.

The proposed explanation for the more unsteady and significantly different behavior is that the acoustic modes contribute to the shock motion together with the boundary layer disturbances, when the flow is not choked. If they are of comparable strength, they may interact with each other and thus create a quite different perturbation profile compared to the case when the boundary layer disturbances dominate.

Flow decomposition was carried out for Case 6 in order to gain insight into the three-dimensional characteristics of the interaction, something which is very difficult when using two and one-point correlations. The DMD mode spectra can be observed in Figure 7.5 zoomed in to the St_L range of 0.02 - 0.05 suggested by Dussauge et al.Dussauge *et al.* (2006) to be typical for SBLI. where the magnitude of the DMD modes are computed by normalizing the modes,

$$\boldsymbol{\phi}_{j,\text{norm}} = \mathbf{U}_1^m \|\mathbf{W}\boldsymbol{\Sigma}^{-1}\widetilde{\boldsymbol{\psi}}_j\|, \tag{7.1}$$

compare to Equation 5.35, and then computing the L2-norm of the $\boldsymbol{\phi}_{j,\text{norm}}$.

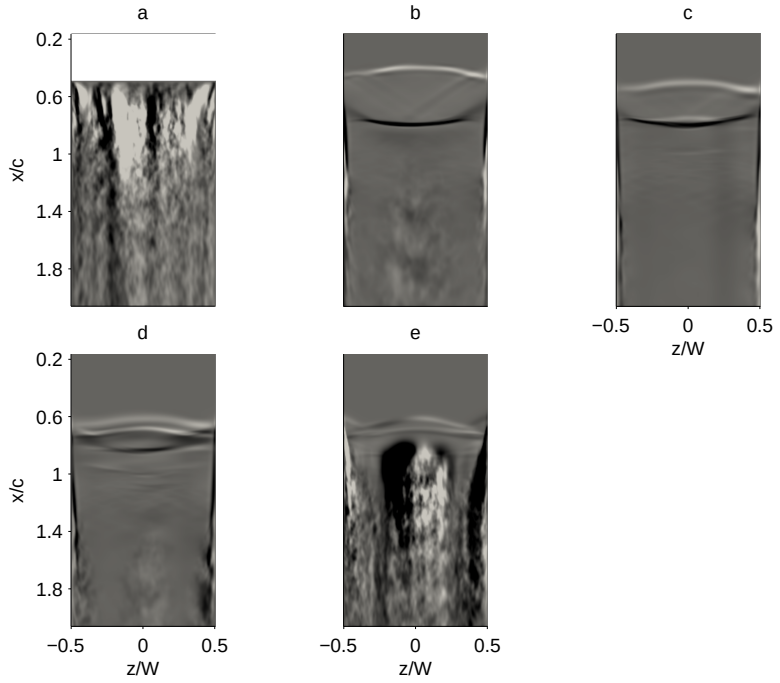

FIGURE 7.6. DMD mode 5, $St_L = 0.024$. Slices of streamwise velocity ,U_x, parallel to roof and floor, scale is from -5 (black) to 5 (white).

The modes are here numbered by their L_2 norm from mode 1 and forwards. Mode 0 is the most energetic mode of the decomposition but corresponds to the mean field and thus is not included in the DMD spectra, Figure 7.5. The fifth mode has a frequency of $St_L = 0.024$ (63 Hz) and is the most energetic mode in the St_L range of interest. Furthermore, it agrees well with the previous analysis using the coherence function which found a frequency of $St_L = 0.025$ for the simultaneous movement of floor and roof shock feet. The mode shape can be observed in Figure 7.6 where it is visualized by spanwise cuts of the channel, see Figure 7.5. The mode of the shock system can be observed in pictures (b) and (c) of Figure 7.6 and consist of opposing movement between the terminating shock and the upstream part of the system creating a breathing, or bellows-like movement. The flow separation from the floor, visible in picture (a) of Figure 7.6, show larger portions of downstream flow compared to upstream flow. The roof separation, picture (e), show up- and downstream flow side-by-side in approximately equal amounts.

There is a low frequency component in the separated flows without shocks which is often called flapping, see for example Kiya & Sasaki (1985), Driver *et al.* (1987) and Lee & Sung (2002).

It has been proposed that the flapping is associated with an imbalance between the entrainment of fluid through the shear layer and the outflow of fluid at the reattachment point leading to a build-up of fluid in the bubble. This build-up will eventually cause the bubble to have a swift collapse of the entire bubble which releases the built-up fluid, followed by reinstatement of the recirculation at a slower pace. Heenan & Morrison (1998) managed to attenuate the flapping in subsonic separated flow by introducing a permeable surface under the recirculation and thus allowing fluid to flow in and out of the separation bubble which will compensate for this mass flow imbalance. The effect of the permeable surface was an effective removal of the flapping instability which, while it does not prove the proposed mechanism true, it at least confirms the validity as a explanation model.

Observation of the mode shape of Mode 5 show that the regions of reverse flow are significantly smaller compared to the regions of stream-wise flow which could be an indication that a similar phenomenon is present there. As the DMD mode has a harmonic variation with zero mean, an imbalance between inflow and outflow of fluid in the separation bubble is one possible explanation for the mode shape. The idea is supported by the behavior of the shock system which has the entire width of the shocks moving in unison and opposing direction, something which would happen if the separation bubble has a collapse/reinstatement cycle. If the separation dynamics associated with Mode 5 is the flapping behavior described above, it could be the cause for the characteristic unsteady behavior of SBLI.

7.1.0a. *Forced flow oscillation.* To investigate the response of this sensitive flow to disturbances, periodic excitation at different frequencies was attempted. Excitation by means of varying both the outlet static pressure and the inlet mass flow was investigated, but only the former in a detailed fashion. The reason for this choice is that this is the preferred method of almost all prior investigations of transonic bump flow known to the author, making comparisons more straightforward. The outlet static pressure was varied within the limits of the steady boundary condition investigation in a sinusoidal fashion,

$$p_{out} = p_0 + 0.08p_0 \sin(2\pi f t), \tag{7.2}$$

where p_0 was set to 100 kPa. The excitation frequency was set initially to 5 Hz, but also 10 Hz and 30 Hz was tested.

The position of the shock foot as a function of the outlet pressure can be seen in Figure 7.7), together with mean positions from computations using steady boundary conditions.

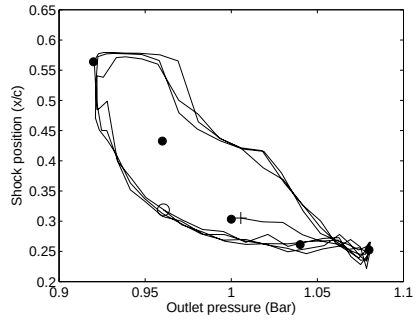

(a) Shock position versus outlet pressure, 5 Hz

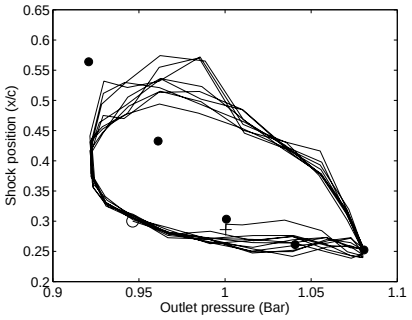

(b) Shock position versus outlet pressure, 10 Hz

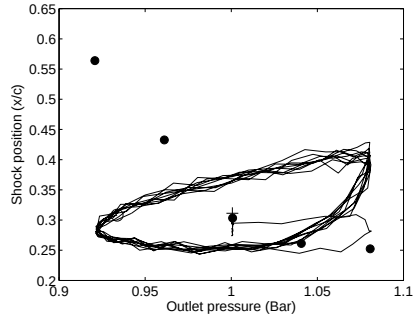

(c) Shock position versus outlet pressure, 30 Hz

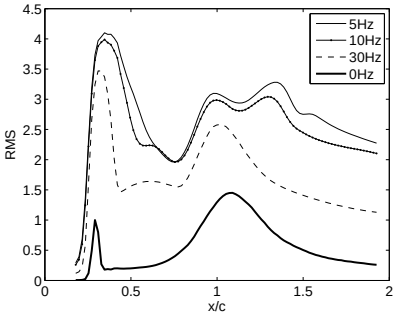

(d) RMS of pressure at bump surface normalized by RMS at shock position for 0 Hz case

FIGURE 7.7. Shock position on the bump surface for 5, 10 and 30 Hz perturbation (a,b,c), the filled circles are mean data from steady boundary condition calculations. RMS of pressure at bump surface for 0, 5, 10 and 30 Hz, (d), normalized by RMS value at shock location for steady boundary conditions.

The shock position shows clear hysteresis for all forcing frequencies. The shape of the shock position traces indicate the formation of a cycle where the shock position depends, for a given back pressure, on if the flow is accelerating or decelerating. When the perturbation frequency is varied the shape of the position trace also varies quite significantly. Comparing the three different plots in Figure 7.7) one can see that the amplitude of the shock motion seems

to decrease as perturbation frequency increases. For 5 and 10 Hz, the deviation from the steady BC data at an outlet pressure of 100 kPa is more significant when the flow is decelerating compared to accelerating flow. In the case of 30 Hz perturbation frequency, the deviation is more or less the same at this point. In general, the 30 Hz case stands out in comparison to the two lower frequencies and must be quite far removed from the quasi-steady regime in which at least the 5 Hz case is located.

If some extrapolation is allowed from the presented data one could make the assumption that, if the perturbation frequency is very low, the trace would be on top of the steady BC data, and, if it was very high there would be no shock motion. In physical terms, the response time of the system is finite and not dependent on the forcing frequency as can clearly be seen in Figure 7.7. If the perturbation frequency is very high, this response time will be too long for the shock system to adjust to the change in conditions leading to the decrease in amplitude which can be observed already at 30 Hz.

The reasoning behind the other perturbation frequency limit is that if the frequency is precisely zero, the flow has stationary boundaries. If the frequency is very low, the flow behavior is likely to be very close to the steady case.

There may however be perturbation frequencies at which the shock behavior deviates from this proposed behavior if resonance in the system occurs. The possibility of resonance exists if the natural oscillation frequency of the shock locks in to the perturbation frequency. The natural oscillation of the shock is quite broad-band and situated at frequencies an order of magnitude above the tested ones, explaining why no resonance has been observed.

Due to practical reasons the low frequency perturbation cases have a smaller amount of recorded periods compared to the high frequency ones. This means that the settling behavior of the position trace at different frequencies can not by evaluated equally and that especially the trace of the 5 Hz case, having only 3 periods of data, is difficult to analyze at all. So, the nature of the trace and the kind of attractor will not be discussed.

To further analyze the data from the forced flow, the RMS of the static pressure along a line on the bump surface in the center of the channel was studied. The data in Figure 7.7 show clearly the difference in the amplitude of the shock oscillation when comparing the different cases in the width of the first peak.

Another clear difference is the maximum of the RMS in the shock peak, and also the different appearance in the reattachment region. All the perturbed cases have a higher RMS at the shock location compared to the separation region while, for the steady BC case it is the opposite. That the RMS levels are much higher for the perturbed cases is quite natural as the amplitudes are naturally higher because of the perturbation.

In order to explain the hysteresis one must first consider a coordinate system in which the shock is at rest. In such a system the motion of the shock, which results from the change of pressure ratio over the domain, will cause a higher shock Mach number when the flow is decelerating and the shock moves upstream and a lower shock Mach number when the shock moves downstream in accelerating flow. This is so because the incoming flow Mach number changes very little over the range of the outlet pressure variation.

This behavior was also observed by Bruce & Babinsky (2008) among others. Due to this behavior, the shock Mach number will depend on the outlet pressure history causing the shock to assume a more upstream position in accelerating flow and vice versa for decelerating flow, compared to steady boundary condition calculations at the same pressure ratio. This behavior also causes the variation in the shock induced separation discussed in Paper 2. The separation is more violent in the decelerating flow because of the higher relative Mach number and hence, stronger shock, compared to both steady boundary condition conditions and accelerating flow.

The total pressure loss is related to shock strength but there are also other sources of viscous losses in the considered flow. The shock Mach number varies between approximately unity and 1.5 so there must be a clear variation in the losses associated with the shock as the outlet pressure varies, something which is evident in the data. The reason for the lack of hysteresis in the total pressure loss is either that the shock strength does not exhibit hysteresis or that the balance of the sources of pressure loss may change as the flow accelerates and decelerates. No attempt has been made to separate the different sources of loss but it is expected that the shock is dominant. Thus, the first suggestion above is the most likely.

7.2. Transonic flow in an model IC engine exhaust valve port

7.2.1. *General observations*

The flows in the model exhaust port for the three cases are qualitatively similar to each other. At the inlet region, the flow is almost stationary at a high static pressure. Near the valve, the flow is rapidly accelerated to a high velocity (supersonic for Cases 2 and 3). After the valve plate, the geometry expands and makes an almost 90° turn while passing the valve stem. At the bend the flow velocity is significantly higher in the outer part. This is the most interesting part of the flow as it exhibits significant unsteady dynamics and is the birthplace of two pairs of counter-rotating vortices, one in the upper part and the other in the lower part of the port, shown in see Figure 7.8.

The vortex pairs are formed by different mechanisms: The lower pair is created by inertial forces and the pressure gradient in the pipe bend while the

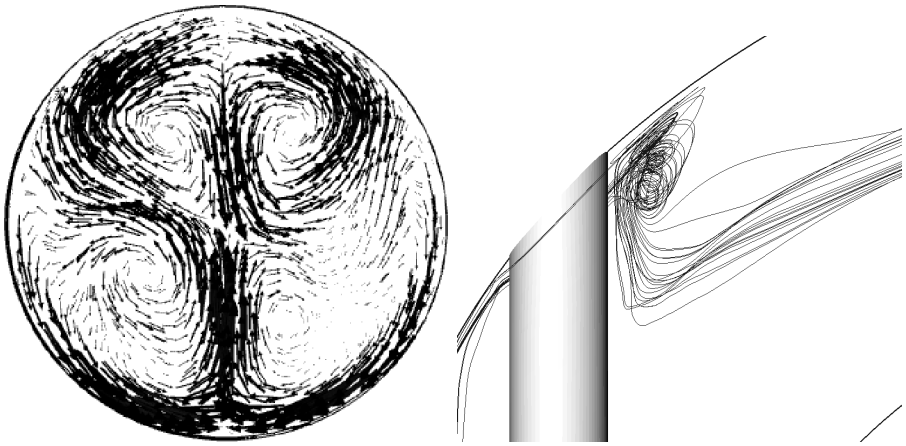

FIGURE 7.8. Left: Instantaneous in-plane velocity vectors one pipe diameter downstream of the valve. Arrows are in-plane velocity, axial flow is into the picture. Right: Streamlines showing the wake behind the valve.

upper pair is created by interaction between the wake behind the valve and the free stream.

The pressure gradient in the bend is directed inwards and the low momentum fluid at the pipe walls are forced in this direction by this gradient. Inertial forces work in the opposite direction, outwards, and the result are the lower pair of vortices.

The wake behind the valve stem can be seen in Figure 7.8, the low-momentum fluid in the wake exits downward in the picture due to the pressure gradient in the pipe. When this fluid interacts with the mean flow, from left to right in the figure, the two upper vortices are created.

7.2.2. *Spectral and correlation analysis*

In order to confirm the general observations made and also make some more quantitative analysis, the power spectral density (PSD) and autocorrelation techniques were used on data recorded along the centerline of the port channel. All data is obtained by first running the simulation for approximately 20 flow-through times and then gather statistics during 20 additional flow-through times. This procedure is used to ensure that the results are free of dependence on the initial conditions, to a reasonable degree.

The dominant peaks in all the spectra can be associated to the valve stem diameter and flow velocity by the Strouhal number. The likely origin of the

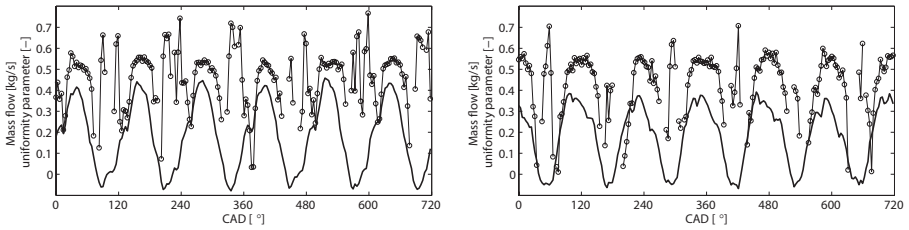

(a) 1200 rpm

(b) 1900 rpm

FIGURE 7.9. Phase averaged turbine inflow massflow, '–', and flow uniformity index, '-o-'.

peaks is the dynamics of the outer vortex pair because of the close connection to the valve stem by the Strouhal number, of order unity, of these peaks.

The correlation analysis show that the disturbances quickly dissipated out for Cases 1 and 3, but survived for Case 2. The cause for this may be that because Case 2 never relaxes back to subsonic flow after the first acceleration the flow is supersonic in the downstream part of the exhaust port. This means that, although losses are higher in this case (even higher than Case 3), there are no disturbances propagating upstream in the core flow who can disturb the structures created at the valve and in the bend. These disturbances may cause the created structures to dissipate faster for the two cases with subsonic flow in the downstream part of the port.

A more detailed analysis, together with figures can be found in Paper 3.

7.3. Flow in a heavy-duty exhaust manifold

The flow in an industrial exhaust manifold was realized for engine-like boundary conditions in order to characterize the structures generated at the turbine inlet. A common tool used by the industry to analyze the flow in manifolds is some form of uniformity index, or parameter. For the investigation carried out here, the form of Equation 5.1 is used to form the flow uniformity index γ. This will reduce the three-dimensional time-dependent flow through a two-dimensional surface to a one-valued function of time. With the boundary conditions for Cases M4 and M5 described in Table 3, corresponding to high load, the phase averaged flow uniformity index at the turbine inlet plane is plotted in Figure 7.9 together with the mass flow. The sensible range of γ is between 0 and 1 where exactly 1 can mean a perfect plug flow where every part of the velocity profile is equal which also include zero velocity. For most applications, zero velocity also means that γ is irrelevant. The most relevant period for the turbine is when the mass flow is high and then, the flow uniformity index is above 0.5.

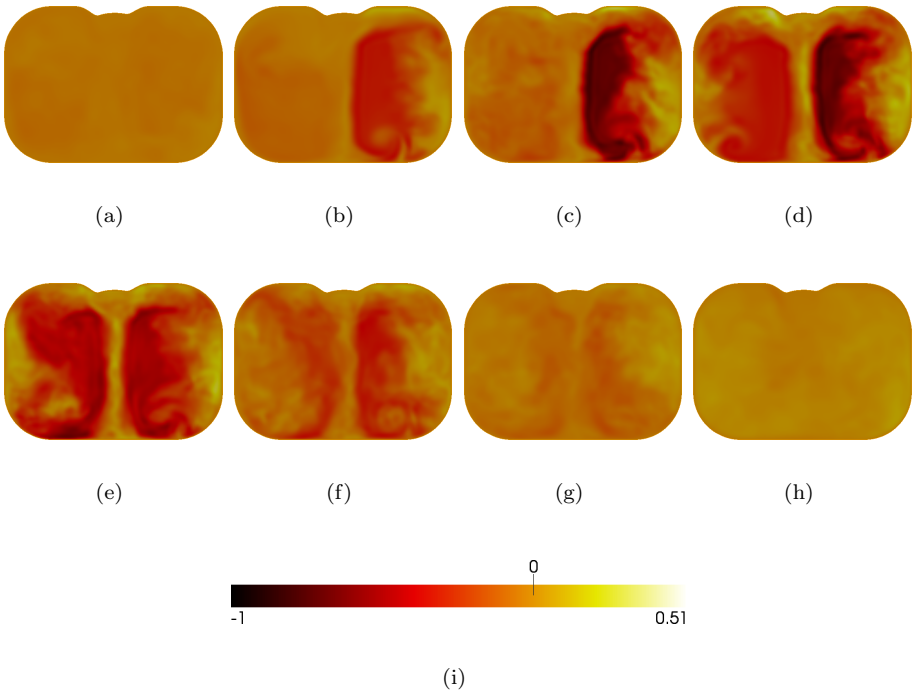

FIGURE 7.10. Phase average velocity component normal to turbine inlet plane for 1200 rpm during the blow-down pulse of cylinder 4. The velocity is normalized by the absolute value of the maximum velocity of that component.

Even though γ provides a quantitative measure, it is impossible to determine what this actually means without knowledge of the actual flow structure. The normalized axial velocity component at the turbine inlet plane is plotted in Figures 7.10 and 7.11 for two different rotational speeds. The range of the images is chosen so that they include one mass flow pulse. The mass flow pulse is built up by two separate sources: The blow-down pulse of cylinder 4 and the scavenging pulse of cylinder 2 (in the particular images displayed). The maximum mass flow, and maximum γ occur when they are both active. In order to quantify which part of the flow is most important in an energy sense, the POD (see Chapter 5) was computed from the simulation data. The POD decomposes a sequence of data into modes that are orthogonal and optimal in an energy sense. This means that it is a good way to remove parts of the flow that contain small amount of energy and focus on the energetic parts that are important for the turbine. The coefficients ($a_j(t)$, see Equation 5.10) of

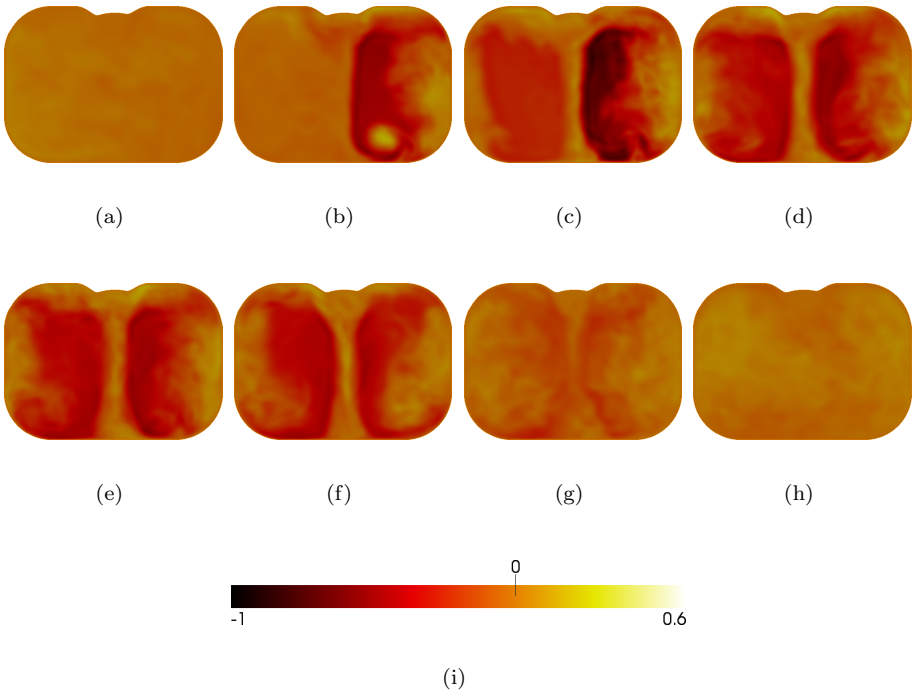

FIGURE 7.11. Phase average velocity component normal to turbine inlet plane for 1900 rpm during the blow-down pulse of cylinder 4. Normalized by the absolute value maximum velocity of the same velocity component.

the first three POD modes of the two cases studied are plotted in Figure 7.12. Studying the behavior of the coefficients both in time and in the frequency domain gives an good indication what the individual modes represent. Not surprisingly, Mode 0 containing more than 67 % of the total kinetic energy of the decomposition is the main mass flow pulse. This can be determined by the characteristics of the coefficient from the two cases, which are very similar, dominated by the firing frequency and strictly positive. The mode shape, ϕ_j, of Mode 0 is plotted in Figures 7.13(a) and 7.14(a) respectively for the two cases. The mode show the qualitative behavior of the manifold at maximum mass flow as previously observed in Figures 7.10 and 7.11 with flow coming from both sides of the manifold.

Mode 1, the second most energetic mode of the manifold, also shows very similar characteristics for the two rotational speeds. This mode has a dominating frequency of half the firing frequency and the harmonics of this. Contrary

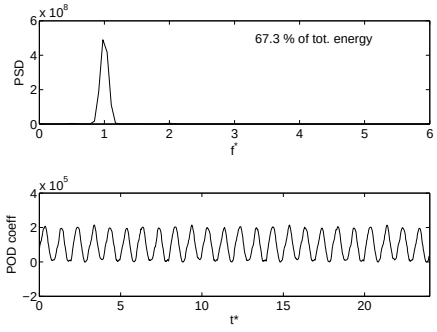

(a) 1200 rpm (DC1), POD Mode 0

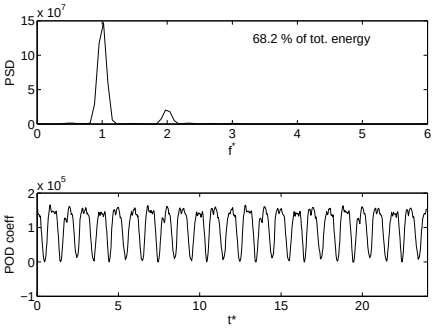

(b) 1900 rpm (DC3), POD Mode 0

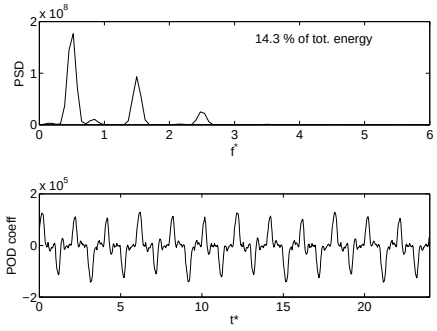

(c) 1200 rpm (DC1), POD Mode 1

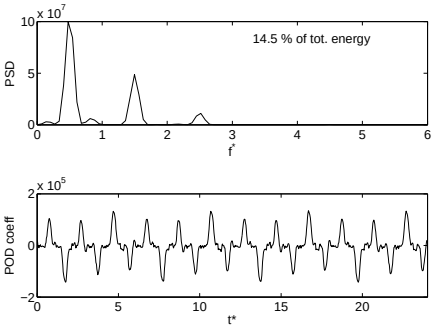

(d) 1900 rpm (DC3), POD Mode 1

FIGURE 7.12. POD coefficients and PSD of POD coefficients.

to $a_0(t)$, $a_1(t)$ is not strictly positive but seems to be rather symmetric around zero. Studying the mode shape of Mode 1 (Figures 7.13(b) and 7.14(b)) it is clear that this mode is describing the side-to-side behavior of the manifold, where the blow-down pulses alternate between coming from the right and left sides of the manifold.

Mode 2 of the POD contain less than 3% of the total kinetic energy of the decomposition and it does not have dynamics (in terms of frequency) that fall in the range of the energetically important modes.

To complement the analysis, the flow data was also treated by Dynamic Mode Decomposition (DMD), see Chapter 5. In contrast to the POD, DMD decomposes based on frequency so that each spatial mode has a unique frequency and growth rate. It is however possible to asses the kinetic energy of

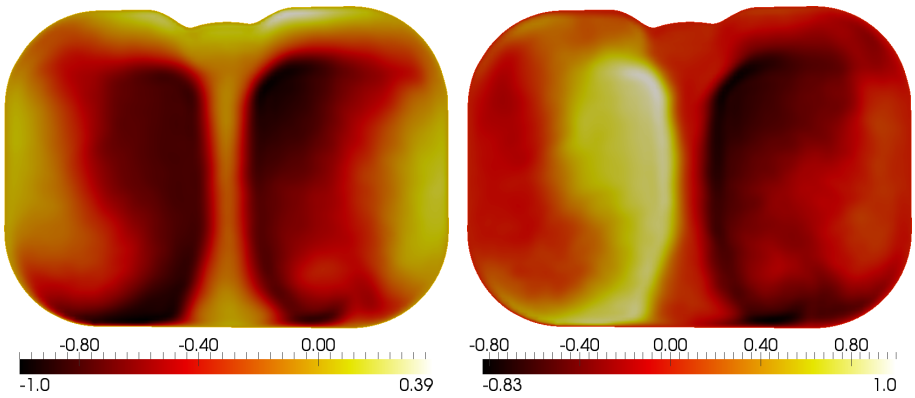

(a) Mode 0 (b) Mode 1

FIGURE 7.13. POD modes 0 and 1 for 1200 rpm (DC1). Normalized by maximum absolute value.

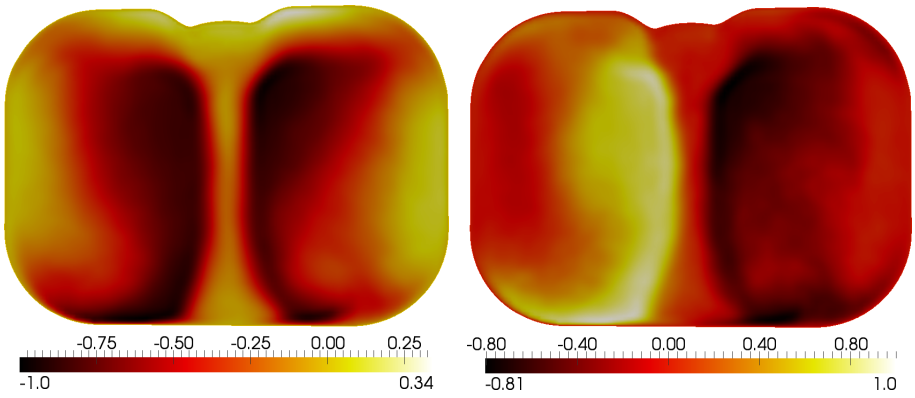

(a) Mode 0 (b) Mode 1

FIGURE 7.14. POD modes 0 and 1 for 1900 rpm (DC3). Normalized by maximum absolute value.

the DMD modes in relation to the total energy of the snapshot sequence by first normalizing the modes like in Equation 7.1, and then computing the L2-norm of the $\boldsymbol{\phi}_{j,\text{norm}}$. By doing this one may rank the DMD modes by kinetic energy so that Mode 0 is the most energetic, Mode 1 the second most energetic and so on. This normalization does not change the shape of the DMD modes, only

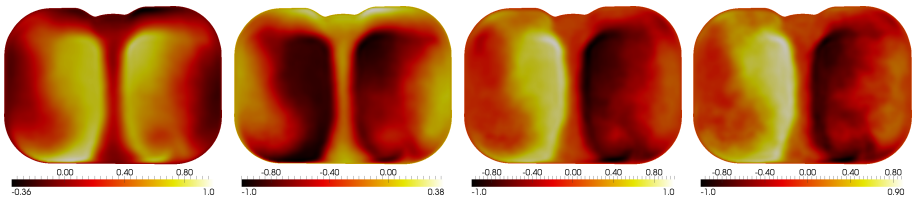

(a) Mode 0, $f^* = 0$ (b) Mode 1, $f^* = 1$ (c) Mode 2, $f^* = 0.5$ (d) Mode 3, $f^* = 1.5$

FIGURE 7.15. DMD modes 0-3 for 1200 rpm.

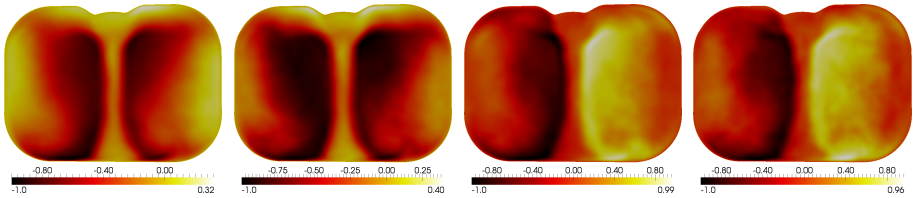

(a) Mode 0, $f^* = 0$ (b) Mode 1, $f^* = 1$ (c) Mode 2, $f^* = 0.5$ (d) Mode 3, $f^* = 1.5$

FIGURE 7.16. DMD modes 0-3 for 1900 rpm.

their magnitude, and provides a way of sorting the modes by using the same quantity as the POD.

Using this ordering, the DMD modes 0 to 3 are plotted in Figures 7.15 and 7.16. For both rotational speeds, the most energetic DMD modes have frequencies found in the two most energetic POD modes but, there is no one-to-one correspondence between POD and DMD modes. Each POD mode is instead represented by the sum of two DMD modes. That the most energetic mode has zero frequency and represent a mean flow is perhaps surprising with the POD results in mind: The most energetic mode was a pulsating flow (strictly positive coefficient $a_0(t)$). By the nature of the DMD, this kind of behavior can not be captured in only one mode because the time variation must be harmonic with a constant growth rate. The pulsating flow must therefore be split into two modes, one with zero and the other with the firing frequency who together correspond to POD Mode 0.

POD Mode 1, with a dominating frequency of $f^* = 0.5$ and harmonics at $f^* = 1.5$ and $f^* = 2.5$ correspond to DMD Mode 2 and 3, if the second

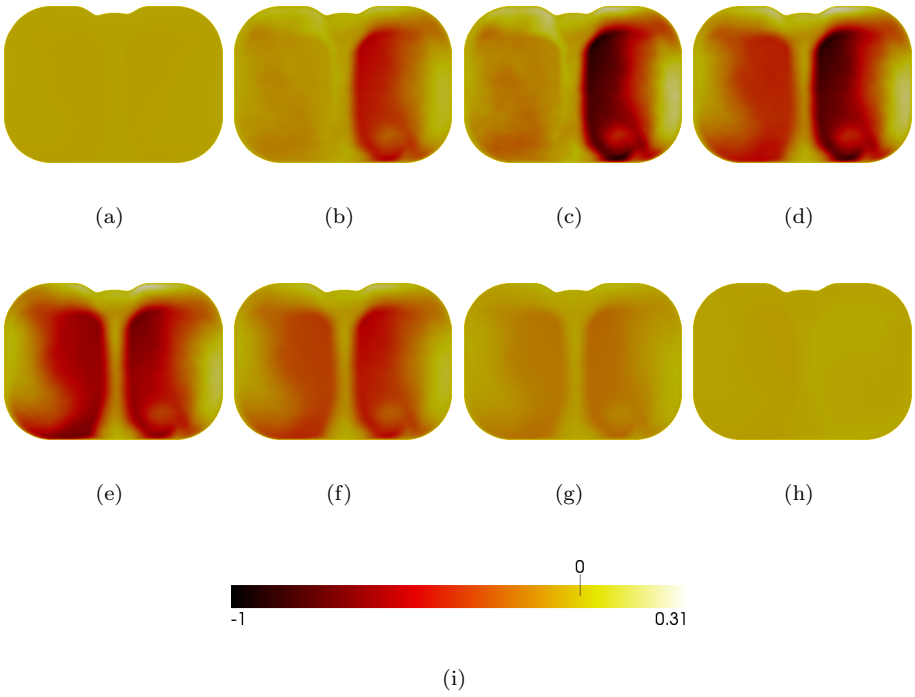

FIGURE 7.17. POD reconstruction using 3 modes (85% of total energy)

harmonic is excluded. To describe the basic flow, Mode 2 is enough as it describe the alternating side-to-side flow dynamics of the manifold.

As the POD is based on energy directly, it is possible to make low-order representations of a snapshot sequence in a straight-forward manner. This will here be used as a filter to reconstruct an exhaust event like those in Figures 7.10 and 7.11 with only the most energetic parts of the flow present. Plotted in Figure 7.17 is a reconstruction using the three most energetic modes of the POD. Using three POD modes means, in this case, that 85% of the total kinetic energy of the snapshot sequence is included in the reconstruction. Studying the images, it is clear that the main dynamics of the flow is included and that three modes are enough to describe the main features at the turbine inlet plane.

CHAPTER 8

Summary and conclusions

The work presented in this thesis consist of Large Eddy Simulations of the transonic flow past a bump and in a model IC engine exhaust valve port as well as investigations of the flow in an exhaust manifold with engine-like geometry and boundary conditions. The thesis also includes descriptions of the computational tools used for the simulations set-up and a presentation of the data analysis methods employed. This chapter contains conclusions based on the results from Chapter 7 and some comments on possible future work.

8.1. Transonic channel flow

The purpose of this investigation was to increase the understanding of the natural and forced unsteadiness of the shock system in transonic channel flow. This study was carried out as a pre-study of the flow past IC-engine valves at near opening and closing positions. The results from the investigation of transonic flow past a bump show that a subsonic inflow is accelerated to supersonic velocity as it passes the bump for low enough outlet pressure and that a shock system is formed, terminating the supersonic region. The formation of a shock leads to shock-induced separation of the incoming boundary layer due to the large pressure gradient over the shock. Primarily due to a strong coupling of the shock and separation dynamics, the shock system is always unsteady. The nature of the interaction was investigated by Dynamic Mode Decomposition showing a mode at $St_L = 0.025$. The mode corresponding to the recirculation zone and can be interpreted as showing the periodic growth and collapse of the recirculation bubble. The flow is highly sensitive, making small changes in the boundary conditions result in significant variations in the shape and type of shock system as well as separation appearance. The shock system position exhibit a hysteretic behavior when the outflow pressure was varied with a low frequency. This behavior is due to differences in shock Mach number in accelerating and decelerating flow.

8.1.1. *Proposed future work*

While the results clearly show that the recirculation zone is responsible, further investigation is still necessary to determine the exact nature of the driving

structure. Understanding the relation to the low-frequency flapping would greatly benefit from a more detailed investigation of the flapping phenomenon which may be more easily done for a subsonic separation.

8.2. Transonic flow in a model IC engine exhaust valve port

The purpose of this investigation was to increase the understanding of the flow in exhaust ports with regard to generation of coherent structures and flow unsteadiness. The investigation of a model exhaust port shows that at realistic pressure ratios, transonic flow is reached. The flow in the considered geometry was found to be highly unsteady, something which is expected also in industrial geometries. For all computed cases, two pairs of vortices are created in the exhaust port by interaction with the valve stem and by inertial effects and the pressure gradient in the pipe bend. The mechanisms responsible for the creation of the vortical structures observed in the flow are such that they can be expected to be present also in other port geometries. The pairs are located in the top and bottom parts of the exhaust port, respectively. The upper vortices, originating in the interaction with the wake behind the valve stem is responsible for the main unsteadiness in the flow while the lower pair has low momentum and are thought to not be driving the unsteadiness. The spectral and correlation investigations confirm periodical motion originating in the wake interaction and show that the periodical structures quickly dissipate.

8.2.1. *Proposed future work*

The port investigation would benefit from experimental results under engine-like conditions. The main point of such side by side simulations and experiments are not a one to one matching of quantitative results but to let the respective merits of the approaches complement each other. This could expand the qualitative and phenomenological knowledge base regarding the flow in the exhaust port.

In this thesis, the effect of valve movement is considered to be of secondary importance based on comparison of the velocities of fluid and valve. While true for typical peak fluid and valve velocities, it is not necessarily true for very small lifts at the beginning of the blow-down pulse. Determining the effect of valve motion on flow losses and structure generation remains to be addressed.

A number of simplifications are assumed regarding boundary conditions in the valve port and. The value of the results would be increased by an expanded study of the effect of secondary flows at the inlet as well as pressure disturbances coming from the outlet. Furthermore, the effect of non-smooth walls on losses and flow structure generation are not investigated.

8.3. Flow in a heavy-duty exhaust manifold

The purpose of this investigation was to characterize the flow at the turbine inlet plane of a heavy-duty exhaust manifold under engine-like boundary conditions. The characterization was carried out primarily by POD and DMD and the merits of these decomposition methods for the acquired results were also evaluated. The strongest flow structure at the turbine inflow plane was found to be a combination of the blow-down pulse coming from one cylinder, and the scavenging pulse from another at the firing frequency. POD capture this behavior in one mode (Mode 0) while DMD do so in the two modes, the sum of Mode 0 and 1. The dominating dynamics at the turbine inlet are captured by only 2 and 4 modes for POD and DMD, respectively. No significant dependence on rotational frequency was found for the strongest modes, neither for POD nor DMD. The decomposition parameter variations show that POD is essentially insensitive and that DMD show small qualitative differences in response to this. Care should be taken the analyzing the DMD results based on the energy content of the normalized modes as the decomposition is based on frequency and growth rate. Very long sampling times are necessary for near zero growth rate DMD modes in flow cases of the type investigated here.

8.3.1. *Proposed future work*

In the same manner as for the port, the manifold results would benefit from experimental results under engine-like conditions.

A number of simplifications are done regarding boundary conditions in the manifold. The value of the results would be increased by an expanded study of the effect of secondary flows at the inlet, pressure disturbances coming from the outlet and wall roughness.

The manifold flow investigation is motivated by the desire to increase the understanding of the structures generated by the manifold. It is known that the structure at the turbine inflow will have an effect on the turbine efficiency. However, the actual mechanism by which the structures affect the turbine is not fully known. More fundamental research into this aspect of turbine/manifold interaction is needed.

CHAPTER 9

Papers summary and authors contributions

Paper 1

Shock unsteadiness and shock induced separation at transonic flows over a bump.
O. Bodin & L. Fuchs.
ETMM7 proc. p. 720, 7th International Symposium on Engineering Turbulence Modeling and Measurements, Limassol Cyprus 2008

The purpose of the work is to investigate the dynamics of the unsteady flow in the transonic wind tunnel. The paper discusses the interaction between the shock and the unsteady boundary layer. The work was performed by Bodin under supervision by Fuchs. The results were presented at the 7th International Symposium on Engineering Turbulence Modeling and Measurements, Limassol Cyprus 2008 by Bodin.

Paper 2

Shock motion and shock induced separation in oscillating pressure driven transonic flow over a bump.
O. Bodin & L. Fuchs.
AIAA 2008-4174. 38th AIAA Fluid Dynamics Conference and Exhibit, 23 - 26 Jun 2008, Seattle, Washington USA.

The purpose of the work is to investigate the dynamics of the unsteady flow in the transonic wind tunnel with oscillatory driving pressure gradient. The main emphasis is on the shock dynamics. The work was performed by Bodin under supervision by Fuchs. The results were presented at the 38th AIAA Fluid Dynamics Conference and Exhibit, 23 - 26 Jun 2008, Seattle, USA.

Paper 3

Transonic flow in IC engine exhaust valves.
O. Bodin & L. Fuchs.
ICJWSF2, 2008, Berlin, Germany.

Transonic flow in a model exhaust port is investigated. Flow structures are characterized and their likely origin are discussed. The work was performed by Bodin under supervision by Fuchs.

Paper 4

LES of the exhaust flow in a heavy-duty engine
O. Bodin, Y. Wang, M. Mihaescu & L. Fuchs.
LES4ICE, November 2012.
Submitted to Oil & Gas Science and Technology

The flow in a heavy-duty engine exhaust manifold and port was investigated. The work was performed by Bodin and Wang under supervision by Mihaescu and Fuchs. The work was presented at LES4ICE, November 29-30, Paris France.

Paper 5

Analysis of transonic shock/boundary-layer interaction by spectral methods
O. Bodin, M. Mihaescu & L. Fuchs.
Submitted to AIAA Journal.

Transonic shock/boundary-layer interaction is investigated by spectral methods in order to improve understanding of the interaction. The work was performed by Bodin under supervision by Mihaescu and Fuchs.

Paper 6

Analysis of the flow structures in the exhaust manifold of a heavy duty engine
O. Bodin, Mihai Mihaescu & L. Fuchs.
Submitted to Applied Energy.

The flow in a heavy-duty manifold under engine-like flow conditions were investigated by Proper Orthogonal Decomposition (POD) and dynamic mode decomposition (DMD). The work was performed by Bodin under supervision by Mihaescu and Fuchs.

Acknowledgments

First of all I would like to thank my supervisor, Professor Laszlo Fuchs: For your patience and willingness to share your knowledge in fluid mechanics and research but also for consulting on my medical issues and having an opinion on just about everything.

My second supervisor, Dr Mihai Mihaescu: Unfortunately you came into the project only one year ago. Your enthusiasm, knowledge and perspective has been a very positive addition to the project and I wish you would have started at KTH earlier.

Fredrik Hellström, I do not think I would have stayed very long if you had not been there at the beginning. Dr. Nils Tillmark, I am very grateful for all your help. Ramis and Bengt, you have been my go-to guys for everything practical. Emma, you have been the encyclopedia of EDGE. Thank you all!

All the friendly people at the mechanics lab, thank you for all the discussions over coffee or lunch, from European economy to the silver bible and Luxor obelisk. Keep it up with the coffee breaks and enjoy your *Tekniska Gondolen* in my absence!

This PhD project was funded by the CCGEx competence centre. *Stiftelsen Erik Petersohns minne* is acknowledged for funding the participation in AIAA 38. The computational resources was allocated through SNAC and located at PDC, NSC, LUNARC and HPC2N.

My own family has doubled in size during the course of this project. Fia, Isak and Teo, you have been on the receiving end of my anxieties and irregular working schedule during this project and have pulled trough, I love you. Mamma, Pappa, Erik, Anna, Jappe, Petra, Jonas and Markus thank you thank you for stepping in and allowing me to work (and rest) more than would have been otherwise possible.

Bibliography

Agrawal, G., Kaisare, N. S., Pushpavanam, S. & Ramanathan, K. 2012 Modeling the effect of flow mal-distribution on the performance of a catalytic converter. *Chemical Engineering Science* **71**, 310–320.

Anderson, J. D. 2003 *Modern compressible flow, third edition*. McGraw-Hill.

Ben-Dor, G. 1999 Hysteresis phenomena in shock wave reflections in steady flows. *Journal of Materials Processing Technology* **85**, 15–19.

Ben-Dor, G., Ivanov, M., Vasiliev, E. I. & Elperin, T. 2002 Hysteresis processes in the regular reflection Mach reflection transition in steady flows. *Progress in aerospace sciences* **38**, 347–387.

Beresh, S., Clemens, N. & Dolling, D. 2002 Relationship Between Upstream Turbulent Boundary-Layer Velocity Fluctuations and Separation Shock Unsteadiness. *AIAA Journal* **40**, 2412–2422.

Bicen, A. F., Vafidis, C. & Whitelaw, J. H. 1986 Steady and Unsteady Air Flow Through an Intake Valve of a Reciprocating Engine. *Tech. Rep.*. Department of Energy, Washington, DC. DOE/NBM-6005208.

Bogar, T. J., Sajben, M. & Kroutil, J. C. 1983 Characteristic frequencies of transonic diffuser flow oscillations. *AIAA Journal* **21, no 9**, 1232–1240.

Boree, J., Maurel, S. & Bazile, R. 2002 Disruption of a compressed vortex. *Physics of Fluids* **14** (7), 2543.

Bron, O. 2003 Numerical and experimental study of the Shock-Boundary Layer Interaction in Transonic Unsteady flow. PhD thesis, Dept. Energy Technology, KTH.

Bruce, P. J. K. & Babinsky, H. 2008 Unsteady shock wave dynamics. *Journal of Fluid Mechanics* **603**, 463–473.

Buschbeck, M., Bittner, N., Halfmann, T. & Arndt, S. 2012 Dependence of combustion dynamics in a gasoline engine upon the in-cylinder flow field, determined by high-speed PIV. *Experiments in Fluids* .

Caton, J. A. & Heywood, J. B. 1981 An experimental and analytical study of heat transfer in an engine exhaust port. *International Journal of Heat and Mass Transfer* **24** (4), 581–595.

CD-Adapco 2011 StarCCM+ User Guide 6.06.017. *Tech. Rep.*.

Celik, I. B. 2005 Procedure for estimation and reporting of dicretization errors in CFD applications. *Tech. Rep.*. Mechanical and Aerospace engineering department, West virginia university, Morgantown Wv, USA.

Délery, J. M. 1983 Experimental investigation of turbulence properties in transonic shock/boundary-layer interaction. *AIAA Journal* **21, no 2**, 180–185.

Driver, D. M., Marvin, J. G. & Seegmiller, H. L. 1987 Time-dependent behavior of a reattaching shear layer. *AIAA Journal* **25**, 914–919.

Dussauge, J., Dupont, P. & Debieve, J. 2006 Usteadiness in shock wave boundary layer interactions with separation. *Aerospace Science and Technology* **10**, 85–91.

Dussauge, J. & Piponniau, S. 2008 Shock/boundary-layer interactions: Possible sources of unsteadiness. *Journal of Fluids and Structures* **24**, 1166–1175.

Ehrlich, D., Lawless, P. & Fleeter, S. 1997 On-engine Turbocharger turbine inlet flow characterization. In *48th Earthmoving Industry Conference & Exposition*. Society of Automotive Engineers, 400 Commonwealth Dr, Warrendale, PA, 15096, USA,.

Eliasson, P. 2001 EDGE, a NavierStokes Solver for Unstructured Grids. *Tech. Rep.*. Scientific Report FOI-R–0298–SE, Computational Aerodynamics Department, Aeronautics Division, FOI.

Fogleman, M., Lumley, J., Rempfer, D. & Haworth, D. 2004 Application of the proper orthogonal decomposition to datasets of internal combustion engine flows. *Journal of Turbulence* **5** (August 2012), 37–41.

Galindo, J., Luján, J., Serrano, J., Dolz, V. & Guilain, S. 2004 Design of an exhaust manifold to improve transient performance of a high-speed turbocharged diesel engine. *Experimental Thermal and Fluid Science* **28** (8), 863–875.

Galli, A., Corbel, B. & Bur, R. 2005 Control of forced shock-wave oscillation and separated boudary layer interaction. *Aerospace Science and Technology* **9**, 653–660.

Galloway, R. L. 2010 *The Steam Engine and Its Inventors - A Historical Sketch*. Read Books Design.

Ganapathisubramani, B., Clemens, N. & Dolling, D. 2007 Effects of upstream boundary layer on the unsteadiness of shock-induced separation. *Journal of Fluid Mechanics* **585**, 369–394.

Ganapathisubramani, B., Clemens, N. & Dolling, D. 2009 Low-frequency dynamics of shock-induced separation in a compression ramp interaction. *Journal of Fluid Mechanics* **636**, 397–425.

Garmann, D., Visbal, M. & Orkwis, P. D. 2012 Comparative Study of Implicit and Subgrid-Scale Model LES Techniques for Low-Reynolds Number Airfoil Applications. *International journal for numerical methods in fluids* .

Gault, R., Thornhill, D., Fleck, R., Mackey, D. & Chatfield, G. 2004 Analysis of the steady flow characteristics through a poppet valve. *SAE transactions* **113** (3), 1080–1093.

Grinstein, F. F., Margolin, L. G. & Rider, W. J. 2007 *Implicit Large Eddy Simulation: Computing Turbulent Fluid Dynamics*. Cambridge University Press.

Hansen, C. D. & Johnson, C. R. 2004 *Visualization Handbook*. Elsevier Science.

Heenan, A. J. & Morrison, J. F. 1998 Passive control of pressure fluctuations generated by separated flow. *AIAA Journal* **36**, 1014–1022.

Hellström, F. & Fuchs, L. 2008 Effects of inlet conditions on the performance of a radial turbine. In *ASME Turbo Expo*.

Heywood, J. B. 1988 *Internal Combustion Engine Fundamentals*. McGraw-Hill.

Holmes, P., Lumley, J. L. & Berkooz, G. 1998 *Turbulence, Coherent Structures, Dynamical Systems and Symmetry*. Cambridge University Press.

Hornung, H. G. & Robinson, M. L. 1982 Transition from regular to Mach reflection of shock waves part 2. The steady flow criterion. *Journal of Fluid Mechanics* **123**, 155–164.

Hornung, H. G. & Taylor, J. R. 1982 Transition from regular to Mach reflection of shock waves part 1. The effect of viscosity in the pseudosteady case. *Journal of Fluid Mechanics* **123**, 143–153.

Humble, R. A., Scarano, F. & van Oudheusden, B. W. 2009 Unsteady aspects of an incident shock wave/turbulent boundary layer interaction. *Journal of Fluid Mechanics* **635**, 47–74.

Jameson, A., Schmidt, W. & Turkel, E. 1981 Numerical solution of the Euler equations by finite volume methods using Runge-Kutta time stepping schemes (81-1259).

Jeong, J. & Hussain, F. 1995 On the identification of a vortex. *Journal of Fluid Mechanics* **285**, 69–94.

Kalpakli, A., Örlü, R. & Alfredsson, P. H. 2011 Dean vortices in turbulent flows: rocking or rolling? *Journal of Visualization* **15** (1), 37–38.

Karvounis, E. & Assanis, D. N. 1993 The effect of inlet flow distribution on catalytic conversion efficiency. *International Journal of Heat and Mass Transfer* **36** (6), 1495–1504.

Kistler, A. L. 1964 Fluctuating Wall Pressure under a Separated Supersonic Flow. *The Journal of The Acoustical Society of America* **36**, 543–550.

Kiya, M. & Sasaki, K. 1985 Structure of large-scale vortices and unsteady reverse ow in the reattaching zone of a turbulent separation bubble. *Journal of Fluid Mechanics* **154**, 463–491.

Lee, I. & Sung, H. 2002 Multiple-arrayed pressure measurement for investigation of the unsteady flow structure of a reattaching shear layer. *Journal of Fluid Mechanics* **463**, 377–402.

Lee, K. H., Ryu, J. D., Lee, C. S. & Reitz, R. D. 2005 Effect of intake port geometry on the in-cylinder flow characteristics in a High Speed DI Diesel Engine. *International Journal of Automotive Technology* **6(1)**, 1.

Lee, L. L. 1969 A simple formula for the shock polar. *AIAA Journal* **7 no.5**, 985.

Liu, X. & Squire, L. C. 1988 An investigation of shock/boundary-layer interactions on curved surfaces at transonic speeds. *Journal of Fluid Mechanics* **187** (-1), 467–486.

Lumley, J. L. 1967 The Structure of Inhomogeneous Turbulent Flows. In *Atmospheric turbulence and radio propagation* (ed. A. M. Yaglom & V. I. Tatarski), pp. 166–178. Moscow: Nauka.

MAN Diesel & Turbo 2012 mandieselturbo.com.

Mezić, I. 2005 Spectral properties of dynamical systems, model reduction and decompositions. *Nonlinear Dynamics* **41**, 309–325.

Moroianu, D., Caraeni, D. A. & Fuchs, L. 2005 Large Eddy Simulation of a Shock Boundary Layer Interaction in a Transonic Internal Flow. AIAA-2005-0312.

Olsson, M. & Fuchs, L. 1998 Large Eddy Simulation of a forced semi-confined circular impinging jet. *Physics of Fluids* **10**, 476–486.

Persoons, T., Van den Bulck, E. & Fausto, S. 2004 Study of pulsating flow in close-coupled catalyst manifolds using phase-locked hot-wire anemometry. *Experiments in Fluids* **36** (2), 217–232.

Poggie, J. & Smits, J. 2001 Shock unsteadiness in a reattaching shear layer. *Journal of Fluid Mechanics* **429**, 155–185.

Pope, S. B. 2000 *Turbulent flows*. Cambridge university press.

Reynolds, O. 1883 An experimental investigation of the circumstances which determine whether the motion of water in parallel channels shall be direct or sinuous and of the law of resistance in parallel channels. *Proceedings of the Royal Society of London* **35**, 84–99.

Reynolds, O. 1885 On the Dynamical Theory of Incompressible Viscous Fluids and the Determination of the Criterion. *Philosophical Transactions of the Royal Society of London. A* **186**, 123–164.

Rott, N. 1990 Note on the history of the Reynolds number. *Annual review of fluid mechanics* **24**.

Rowley, C. W., Mesic, I., Bagheri, S., Schlatter, P. & Henningson, D. 2009 Spectral analysis of nonlinear flows. *Journal of Fluid Mechanics* **641**, 115–127.

Rutten, F., Schroder, W. & Meinke, M. 2005 Large-eddy simulation of low frequency oscillations of the Dean vortices in turbulent pipe bend flows. *Physics of Fluids* **17** (3), 035107.

Sajben, M., Bogar, T. J. & Kroutil, J. C. 1984 Forced oscillation experiments in supercritical diffuser flows. *AIAA Journal* **22, no 4**, 465–474.

Salasc, S., Barrieu, E. & Leroy, V. 2005 Impact of Manifold Design on Flow Distribution of a Close-Coupled Catalytic Converter. *SAE technical paper* (724).

Salmon, J. T., Bogar, T. J. & Sajben, M. 1983 Laser Doppler Velocimeter measurements in unsteady, separated, transonic diffuser flows. *AIAA Journal* **21, no 12**, 1690–1697.

Schmid, P. J. 2010 Dynamic Mode Decomposition of numerical and experimental data. *Journal of Fluid Mechanics* **656**, 5–28.

Sigfrids, T. 2003 Hot wire and PIV studies of transonic turbulent wall-bounded flows.

Sudo, K., Sumida, M. & Hibara, H. 1998 Experimental investigation on turbulent flow in a circular-sectioned 90-degree bend. *Experiments in Fluids* **25** (1), 42–49.

Thomas, F., Putnam, C. & Chu, H. 1994 On the mechanism of unsteady shock oscillation in shock wave / turbulent boundary layer interactions. *Experiments in Fluids* **18**, 69–81.

Torino, P., Gambarotto, M., Marelli, M. & Scarico, S. 2003 CFD Analysis and Experimental Validation of the Inlet Flow Distribution in Close Coupled Catalytic Converters. *SAE technical paper* (724).

Valentino, G., Kaufman, D. & Farrell, P. 1993 Intake Valve Flow Measurements Using PIV. Fuels and Lubricants Meeting and Exposition, SAE paper 932700.

Versteeg, H. K. & Malalasekera, W. 2007 *An Introduction to Computational Fluid Dynamics: The Finite Volume Method*. Pearson Education Limited.

Wilcox, D. C. 2006 *Turbulence moddeling for CFD*, 3rd edn. DCW Industries.

Wu, M. & Martín, M. P. 2007 Analysis of shock motion in shockwave and turbulent boundary layer interaction using direct numerical simulation data. *Journal of Fluid Mechanics* **594**, 71–83.

Yasar, A., Sahin, B. & Akilli, H. A. 2006 Effect of inlet port on the flow in the cylinder of an internal combustion engine. *Journal of Mechanical Engineering Science* **220**, 73–82.

Zygourakis, K. 1989 Transient operation of monolith catalytic converters: a two-dimensional reactor model and the effects of radially nonuniform flow distributions. *Chemical engineering science* **44** (9), 2075–2086.

Part II

Papers

1

Paper 1

2

Paper 2

Paper 3

3

Paper 4

4

Paper 5

5

Paper 6

6